VIRTUAL AND PHYSICAL PROTOTYPING
2024, VOL. 19, NO. 1, e2396064 (31 pages)
https://doi.org/10.1080/17452759.2024.2396064

Achieving high strength and ductility in Inconel 718: tailoring grain structure through micron-sized carbide additives in PBF-LB/M additive manufacturing

Konrad Gruber[a,b,c], Wojciech Stopyra[a], Karol Kobiela[a], Philipp Kohlwes[b], Jan Čapek[c], Efthymios Polatidis[d] and Ingomar Kelbassa[b,e]

[a]Centre for Advanced Manufacturing Technologies, Faculty of Mechanical Engineering, Wroclaw University of Science and Technology, Wroclaw, Poland; [b]Fraunhofer Research Institution for Additive Manufacturing Technologies IAPT, Hamburg, Germany; [c]Laboratory for Neutron Scattering and Imaging, Paul Scherrer Institute, Villigen, Switzerland; [d]Laboratory of Technology and Strength of Materials, Department of Mechanical Engineering & Aeronautics, University of Patras, Rion, Greece; [e]Institute for Industrialization of Smart Materials, Hamburg University of Technology, Hamburg, Germany

ABSTRACT

Few attempts have been made so far to develop modifiers for in situ use in Inconel 718 PBF-LB/M fabrication. Reports show an increase in tensile strength compared to unmodified counterparts. However, significant ductility reduction is observed, outweighing the mere tensile strength improvements when considering practical applications. In this study, micron-sized powder modifiers (NbC, TiC, and B_4C) were added in proportions of 0.6 wt.% (NbC and TiC) and 0.2 wt.% (B_4C) to Inconel 718 powder for PBF-LB/M processing. These modifiers allowed for grain structure control during heat treatment, including hot isostatic pressing. The addition of NbC resulted in a finer grain structure, while the addition of TiC preserved the as-built grain structure after heat treatment. Carbide precipitates led to uniform GND distribution and promoted uniform stress distribution. We show that the trade-off between strength and ductility in carbide-modified IN718 can be overcome by careful PBF-LB/M processing and heat treatment.

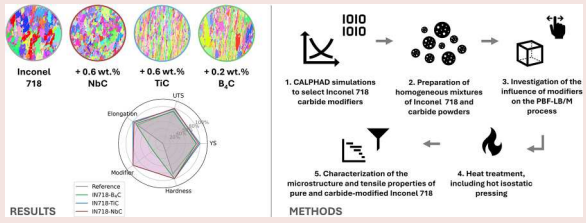

ARTICLE HISTORY
Received 30 May 2024
Accepted 19 August 2024

KEYWORDS
Inconel 718; powder bed fusion; carbides; heat treatment; mechanical properties

1. Introduction

Laser-based powder bed fusion of metals (PBF-LB/M, as defined in the ISO/ASTM 52900 and ISO/ASTM 52911 standards, also known as LPBF, L-PBF, SLM, DLMS) is the most established additive manufacturing (AM) method for the processing of metal alloys [1]. However, metal powder-based AM still faces challenges such as the need for improved materials, in situ monitoring, numerical simulations, productivity, and standardisation, all of which are crucial for the mass production of high-performance parts at reasonable costs [2]. These challenges are particularly relevant in the aerospace sector, where the PBF-LB/M process is often used to produce components from Inconel 718 (IN718). These components typically have lower structural responsibility due to the presence of residual porosity and residual stresses. Hot isostatic pressing (HIP) can reduce the porosity, but it comes with a trade-off – it removes the AM-characteristic cellular-dendritic microstructure and leads to grain size growth and extensive twinning [3].

The mechanical performance of IN718 is limited by its grain size. The typical grain size after the PBF-LB/M process and standard heat treatment process (ASTM F3055-14a, incl. HIP) used by the aerospace industry is equivalent in diameter to ≈100 µm [3], while annealed and aged, forged IN718 is generally characterised by a grain size of ≈20–45 µm [4]. To achieve higher

CONTACT Konrad Gruber konrad.gruber@pwr.edu.pl Faculty of Mechanical Engineering, Wroclaw University of Science and Technology, Lukasiewicza 5 St., 50-371 Wroclaw, Poland

Supplemental data for this article can be accessed online at https://doi.org/10.1080/17452759.2024.2396064.

performance of PBF-LB/M manufactured Inconel 718, ideally matching that of forged materials, a grain control method is essential, allowing the use of PBF-LB/M technology for critical aerospace components. Smaller grain sizes result in more grain boundaries, which act as barriers to dislocation propagation during plastic deformation, thus improving strength. Literature shows strategies for grain refinement, typically through new alloy compositions or process parameter control, such as tilting the build orientation to achieve preferred texture and refined grains based on the as-built crystallographic texture [5].

There are three main methods for the development of new alloys: atomisation, mechanical alloying, and in situ alloying [6]. The current study used in situ alloying, allowing new alloy compositions to be achieved during the PBF-LB/M process [7]. A similar approach is known in conventional casting of nickel superalloys [8,9]. In situ alloying has also been successfully implemented for different reasons within PBF-LB/M, for example, to deal with crack-prone aluminum alloys [10], produce functionally graded titanium composites [11] or reduce grain size in stainless steel [12].

IN718 has been modified with in situ additives such as WC-W_2C [13], $CoAl_20_4$ [14] or MC-type carbides [15–17] during the PBF-LB/M process, achieving significant grain refinement after heat treatment due to the Zener pinning effect. This refinement improves tensile strength and creep resistance. For instance, 2 vol.% ZrB_2 increased room temperature (RT) yield strength (YS) and ultimate tensile strength (UTS) by 12–23% [18], and 2 vol.% SiC by 9–15% [17]. Additionally, 0.5–5 wt.% NbC increased RT YS and UTS up to 15% [16]. Small amounts of TiC and NbC also substantially increased creep rupture life [15], and 2 vol.% ZrB_2 significantly improved high-temperature tensile performance [18]. The influence of B_4C addition on IN718 has not been extensively studied. However, it has been shown that the addition of boron improves the ductility of superalloys by causing serration of the grain boundaries [19]. Boron also improves superalloy creep resistance [20] or fatigue crack growth resistance [21]. Literature also shows examples of IN625-B_4C and IN718-B_4C coatings that lead to improved wear resistance [21,22].

Preliminary studies indicate that improving IN718 properties of with additives such as 2 wt.% ZrB_2 significantly reduces ductility, with a 3-fold decrease in elongation at break at room temperature (RT) and a 2-fold decrease at 650°C [18]. While boron in castings improves high temperature ductility, its effectiveness decreases at high strain rates [19]. Higher boride concentrations can cause microcracks due to mismatched thermal expansion coefficients with the IN718 matrix, increasing local stresses more than at the TiC-IN718 interfaces [23]. Similar reductions in ductility have been observed with 2 vol.% SiC [17], 2 wt.% TiC [24], and 1–2 wt.% TiB_2 [25] at RT. Smaller additions correlate with smaller performance gains, but also smaller reductions in ductility; for example, 0.5 wt.% NbC reduced elongation by 17%, while 5 wt.% reduced it by 623% [16].

The literature presents various strategies for incorporating additives into the PBF-LB/M process. The investigated additive particle size ranges from base powder scale (15–45 µm) [16,23], through micrometer scale (0.5–10 µm) [25,26], to nanometre scale (50–100 nm) [17]. The percentage of additives added ranges from high additions 10–30 vol.% [23,24] to small additions (less than 2 vol.%) [15,27]. Various powder mixing methods are utilised to achieve homogeneous powder mixtures, such as 2-stage high-speed blending, ball milling process [17], two-dimensional rotation blending process (2D mixing) [16], and high-energy ball milling [28]. Non-homogeneous powder mixtures can lead to conglomerates larger than 10 µm with multiple boundaries inside, which form brittle inclusion and promote crack initiation [16]. In general, larger additive sizes and higher fractions of additives require higher melt pool temperatures and longer exposure times to melt the additives during the PBF-LB/M process. If not mixed properly, this will result in metal matrix composites (MMCs), i.e. heterogeneous microstructures. An increase in additive concentration was found to decrease the size of the melt pool [16]. Depending on the PBF-LB/M process parameters, an increase in energy density (ED) can lead to a more homogeneous dispersion of TiC particles in IN718-TiC nano-composites [29]. According to Stokes' formula [28], smaller carbide particles are expected to be captured by the solidification front and distributed within the grains. It has been suggested that larger carbide additives are distributed primarily along the grain boundary (GB) due to the solidification front pushing the carbide particles [30].

Therefore, the design of the alloy composition, the mixing procedure, the process parameters, and other technological factors play a critical role in the final microstructure of the alloy. Studies have shown that microstructures can be tuned to achieve superior hardness [26], or suppress the fraction of Laves phases during solidification compared to pure IN718 due to the consumption of niobium and titanium for carbide formation [31]. Additions such as B_4C can also increase melt pool temperature, suppressing the formation of lack of fusion defects and micropores, as well as refining the microstructure, as shown for B_4C-Inconel 718 [22] and B_4C-Inconel 625 coatings [21]. Other additives introduced in the PBF-LB/M process, such as NbC, lead to a decrease in the average cellular

size, accompanied by a high dislocation density, which contributes to strengthening [16]. Ultimately, additives were introduced to act as nucleation sites, restricting dendritic growth along specific directions during build [26], and restrict grain growth during heat treatment by grain boundary pinning [28]. Adding carbides is a promising method for reducing the adverse effects of HIP and preserving some of the strength properties of as-built IN718.

Studies on pure IN718 have shown that carbides precipitate during PBF-LB/M solidification and grow during heat treatment. However, they do not reduce the ductility of the printed alloy. Precipitated carbides inhibit grain growth during high-temperature heat treatment [32]. Moreover, IN718 alloy can exhibit an elongation at break of 25.9% after high-temperature heat treatment, which is 1.5 times higher compared to the literature average of 16% for PBF-LB/M fabricated and aged IN718 [32]. Among the studies discussed, it was found that the use of carbides, such as NbC, TiC, or SiC, was the most effective. For example, the use of NbC and TiC additives was considered advantageous due to their low wetting angle and semi-coherent interfaces with the γ matrix [16]. Additionally, these carbides are constituent elements of IN718, so any changes introduced in the chemical composition may still fall within the standard. However, to date, studies have shown that in situ added carbides affect the ductility of the IN718 alloy.

The objective of this study was to develop a methodology for grain control of the IN718 alloy after the PBF-LB/M process and a subsequent, including hot isostatic pressing. To achieve this, micron-sized powder additives (NbC, TiC, and B_4C) were added in small weight percentages. The article discusses the influence of carbide powder additives on the properties of IN718-carbide powder mixtures, PBF-LB/M processability, microstructure, and basic mechanical properties. It demonstrates that adding micron-sized carbide modifiers to Inconel 718 powder improves tensile strength through controlled grain structure during heat treatment and uniform stress distribution, without compromising PBF-LB/M processability and ductility.

2. Materials and methods

2.1. Powders

The study uses four types of powder mixtures, three of which were mixtures of reference IN718 and carbide powders, while the fourth consisted solely of pure IN718 and served as a reference. The reference powder was supplied by SLM Solutions Group AG (Lübeck, Germany). The carbide-modified variants were prepared by mixing the base IN718 with micro powders provided by Nanografi Nano Technology (Ankara, Turkey). The percentage of carbide added was determined based on the CALPHAD simulation, which is described later in the study. A proportional weight calculation method was used to determine the additions of carbide powder. Table 1 provides information about the powders.

The chemical composition of powders was measured using an energy-dispersive X-ray fluorescence method (ED-XRF) with a Spectro XEPOS benchtop spectrometer (SPECTRO Analytical Instruments GmbH, Germany) in helium flushing mode. The carbon content in powders as well as PBF-LB/M fabricated samples was determined using a G4 ICARUS (BRUKER, USA) carbon and sulfur analyzer. Each measurement was repeated three times.

2.2. Powder mixing procedure

A custom mixing procedure was used to prepare the powder mixtures. The powders were sieved using a vibratory powder sieve shaker (Fritsch GmbH, Germany) and certified 200 mm/50 µm analytical sieves (Atest sp. z o.o., Poland). Powder mixing was carried out in a V-shaped mixer with a powder chamber volume of 500 ml. All four base powders were sieved through a 45 µm sieve prior mixing. The IN718 sieving was carried out in 1 kg batches for 5 min, while the carbide powders were sieved in 100 g batches for 30 min. Any powder remaining in the sieve was removed from further processing. The sieving process for carbide powder included a second stage of sieving with a 10 µm sieve for 30 min. Any powder remaining on the screen was removed from processing. The base IN718 powder was then mixed with carbide powders in batches using half the volume of the V-shaped powder chamber (250 ml) at a speed of 30 rpm, reversing the direction of rotation every 5 revolutions. Scanning electron microscope (SEM) studies showed that mixing homogeneity is achieved after 20 min. To confirm the homogeneity of the final mixed powders, SEM samples were collected from three different locations within the mixing chamber. Additionally, for each SEM powder sample, three different locations were investigated at different magnifications. The mixed powders were then sieved using 45 µm sieve to remove possible conglomerates. Any excess powder after sieving was removed.

2.3. Powder characterisation

Particle size distribution (PSD) was measured using HELOS BR R4 + RODOS laser diffraction system equipped with VIBRI dispersion unit (Sympatec GmbH, Germany). The powder distribution statistics were analyzed using PAQXOS 3.1 software (Sympatec GmbH, Germany).

Table 1. Powders used in the study and the prepared powder mixtures for PBF-LB/M processing.

Powder	Nominal particle size distribution (µm)	Density (g/cm^3)	Prepared powder mixture	Powder mixture designation
IN718	15–45	8.2	Pure IN718	IN718
NbC	1	7.82	IN718 + 0.6 wt.% NbC	IN718-NbC
TiC	1–3	4.93	IN718 + 0.6 wt.% TiC	IN718-TiC
B_4C	1–3	2.52	IN718 + 0.2 wt.% B_4C	IN718-B_4C

Powder flowability was determined using a Flow Meter SLM powder funnel (SLM Solutions Group AG, Germany) with an opening of 3.81 mm (0.15″) and a cone angle of $\alpha = 30°$. The bulk density was measured using weighted containers filled with the funnel described above. The weights were measured using a laboratory balance of 220 × 0.001 g (Sartorius AG, Germany). Dynamic powder flow was measured using a drum analyzer (Granutools, Belgium). The cohesive index and flow angles were determined as described in [33].

For powder reflectance measurements, a custom setup was used to measure diffuse reflectance of metal powders [34]. The powder was placed inside a BIP 2.0 integrating sphere (B&W Tek, USA), and diffuse light was shone on it using a 20 W tungsten halogen light source. The reflected light was then analyzed using an Exemplar Plus BTC655N-ST spectrometer (B&W Tek, USA) spectrometer. The BIP 2.0 sphere measures light scatter at an angle of 8° to normal (surface of powder sample) – d/8° geometry, and includes the specular component.

2.4. Sample fabrication and heat treatment

A Trumpf TruPrint 1000 PBF-LB/M system (Trumpf GmbH + Co. KG, Germany) equipped with a 200 W fibre laser (wavelength 1,070 nm) and a focus diameter of 55 µm was used for sample fabrication. Two sets of previously optimised parameters for IN718 were tested. The most important process parameters are provided in Table 2.

To investigate the sensitivity of each powder, to the fluctuation of the PBF-LB/M process parameters, a simple 3 × 3 grid search was derived from two base PBF-LB/M parameter sets. The resulting porosity of the sample was chosen as an optimisation criterion. The grid search experiment is presented in Table 3. Energy density was calculated according to equation (1):

$$ED = \frac{P}{v^{*}h^{*}t} \quad (1)$$

where P is laser power (W); v is scanning speed (mm/s); h is hatch distance (mm); t is layer thickness (mm).

In the process of parameter optimisation, cuboidal specimens with dimensions of 5 × 7 × 12 mm^3 were fabricated. In order to study the porosity, metallographic sections were made in the plane parallel to the building direction (BD). Horizontally oriented plates (80 × 4 × 12 mm^3) were fabricated for microstructure investigation and tensile testing. Central set A parameters were used to prepare specimens for microscopy and tensile testing.

The heat treatment parameters are shown in Table 4, and are described in detail in [32]. HT consisted of four steps: stress relief (SR), hot isostatic pressing (HIP), solution annealing (SA), and artificial aging (AA). The HT process is performed using a TAV H3S 1600 vacuum furnace (TAV Vacuum Furnaces SPA, Italy) for SR, SA, and AA, and an EPSI 150-300-2000 hot isostatic press (EPSI NV, Belgium) for HIP. All heat treatments were performed under argon.

2.5. Material characterisation

Metallographic cross sections for porosity and microstructural investigations were embedded in resin, followed by wet grinding using SiC sandpapers, and polishing with 0.05 µm colloidal silica suspension on synthetic polishing cloth. The samples for microstructure studies were etched with fresh Glyceregia (5 ml of HNO_3, 10 ml of glycerol, 15 ml of HCl) for 30–120 s with stirring.

A Keyence VHX 5000 digital microscope (Keyence Corp., Japan) was used to collect stitched images to determine the resulting porosity within the samples. The images were then analyzed with a Python script using Python Imaging Library (PIL 1.1.7). The general microstructure was studied with an Olympus LEXT OLS4000 confocal laser scanning microscope (Olympus Corp., Japan). The Zeiss ULTRA 55 scanning electron microscope (SEM) equipped with EDS detector was used for further microstructure studies (Carl Zeiss AG,

Table 2. Laser powder bed fusion process parameters and scanning strategy.

Set	Layer thickness	Laser power	Scanning speed	Hatch distance	Scanning strategy	Field size (width × depth)	Filling rotation
A	20 µm	165 W	560 mm/s	125 µm	Chessboard	4.1 × 4.1 mm^2	90°
B		160 W	1050 mm/s	55 µm			

Table 3. Experimental grid search – laser powder bed fusion parameter sensitivity study.

Set	Laser power (min)	Laser power step size	Laser power (max)	Scanning speed (min)	Scanning speed step size	Scanning speed (max)
A	155 W	10 W	175 W	510 mm/s	50 mm/s	560 mm/s
B	145 W	15 W	175 W	900 mm/s	150 mm/s	1200 mm/s

Germany). For the Electron Backscatter Diffraction (EBSD) experiment, the SEM was operated at 20 kV in high-current mode with a 120 µm aperture. EBSD raw data was post-processed using the EDAX OIM Analysis 8 software. Carbide size distribution was calculated by binarization of high-contrast SEM micrographs taken using the HDBSD detector (Figure S3 in supplementary material) – average data from 5 random images per variant at 1000x magnification.

2.6. CALPHAD simulations

The equilibrium phase diagram for IN718 and its carbide-modified variants was determined as a function of temperature using the CALPHAD Thermo-Calc software (Thermo-Calc Software AB, Sweden) and the TCNI10 database. A non-equilibrium solidification curve was simulated for the IN718 alloy using the Scheil-Gulliver equation with a cooling rate of $V = 7{\cdot}10^5$ K/s, which corresponds to the cooling rate of PBF-LB/M fabricated IN718, even reaching above 10^6 K/s for some cases [35]. The calculations assumed the chemical composition of IN718, as determined by the ED-XRF measurements presented in Section 3.2. For the modified variants, additions of C, Nb, Ti, and B were calculated according to the proportional weight calculations (Table 1).

2.7. Mechanical properties

Tensile samples were machined from PBF-LB/M fabricated plates with horizontally aligned loading direction. The dimensions of the samples comply with the EN 2002-001:2006 standard and are available in reference [36]. Static tensile tests were carried out at room temperature using an INSTRON 3384 machine (Instron Corp., USA) equipped with a 30 kN load cell and an AVE 2663-821 non-contact video extensometer. The tests were performed at a displacement rate of 0.5 mm/min until the samples fracture. Three samples were tested for each series. A Zwick/Roell ZHVµ-A microhardness tester (Zwick-Roell Group, Germany) was used for the hardness measurements at a load of 9.81 N (1 kgf).

Table 4. Heat treatment parameters used in the study.

Stress relief annealing[a]	Hot isostatic pressing[b]	Solution anneling[c]	Artificial aging[d]
1150°C/6 h	1150°C/4 h/ 150 MPa	1100°C/1 h	720°C/8 h to 620° C/10 h

[a]Samples before cut-off, cooling with furnace under argon; [b]Samples were furnace-cooled under argon and gradually reduced pressure; [c]Cooling under argon at 10 bar abs; [d]Cooling under argon at 1 bar abs.

3. Results and discussion

3.1. CALPHAD simulations

Thermodynamic simulations were used to predict the effects of various additives on the characteristic temperatures of the IN718 alloy. Therefore, the selected additives were considered at 1 wt.% concentration if they did not lower the solidus temperature of the alloy below 1,200°C, as the typical HIP process temperature of IN718 is held at 1,150°C. Based on these criteria, ZrB_2, HfB_2, TiB_2, and TaC were eliminated, while TiC, NbC, and B_4C were selected for further investigations on the effectiveness in grain refinement using the minimum possible fraction. The simulation results showed that dissolving the addition of these carbides in the liquid alloy increases the liquidus temperature and promotes homogeneous nucleation sites in the form of titanium nitrides, titanium carbides, or niobium carbides. Carbides precipitated on the grain boundaries will inhibit grain growth, especially at elevated temperatures of stress relief or HIP treatment, by the Zener pinning mechanism [37]. Therefore, the objective was to determine an additive concentration that would match the liquidus temperatures of both the γ phase and the carbide phase, and increase the carbide phase in the equilibrium state to about 1% for carbide-modified variants from the initial 0.32% for pure IN718. Based on these criteria, the final addition levels were determined at 0.6 wt.% for NbC and TiC and 0.2 wt.% for B_4C (Table 1).

Figure 1(a and b) show the equilibrium state phase diagram and Scheil-Gulliver non-equilibrium solidification curve for the addition of NbC at 0.6 wt.%. The plots for pure IN718, TiC, and B_4C additions are shown in the supplementary material (Figure S1 and S2). The increase in Nb and C results in a significantly higher fraction of the NbC carbide-nitride composite phase (orange line in Figure 1(a)). According to the Scheil-Gulliver curve, the identified phase is NbC carbide grown on TiN nitride. Figure 1(c) shows the chemical composition of the composite phase as a function of the solid fraction, indicating that during the solidification process, the phase is mainly composed of Ti and N. At the end of the solidification

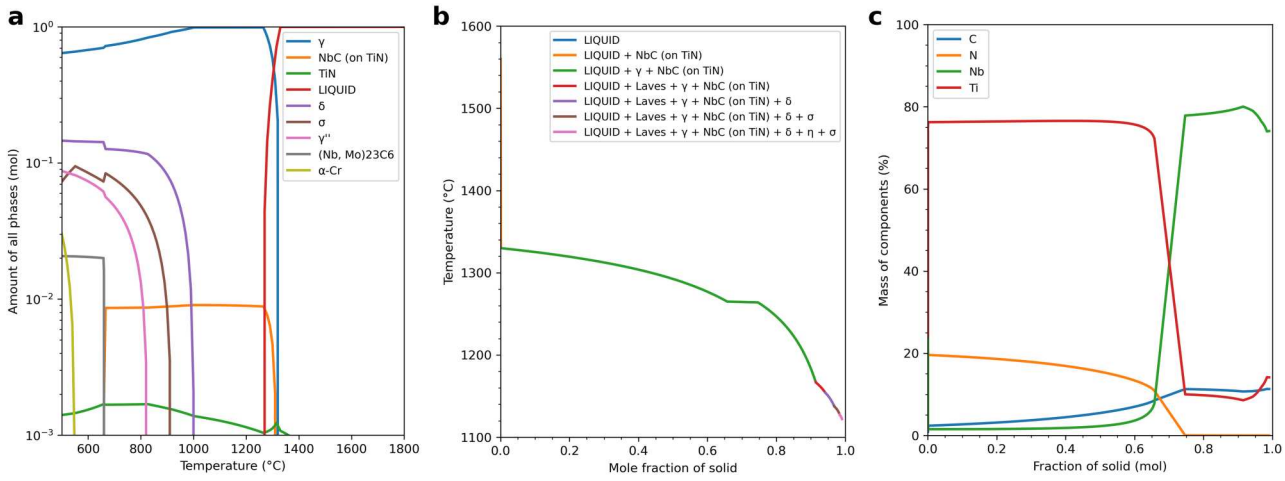

Figure 1. Results of CALPHAD simulation for IN718-NbC; (a) Equilibrium phase diagram; (b) Scheil-Gulliver diagram; (c) Composition of a simulated carbide-nitride composite phase (NbC on TiN).

process, Nb and C become the main elements of the phase. The simulations performed for the non-equilibrium state showed that carbide addition changes the crystallization start temperature and the share of the nucleating phase, which is NbC on TiN. The crystallization start temperatures are as follows: IN718 – 1,555°C, NbC – 1,559°C, TiC – 1,662°C, and B_4C – 1,623°C. The shares of the nucleating phase before the appearance of the γ phase are: IN718 – 0.094%, NbC – 0.101%, TiC – 0.124%, and B_4C – 0.110%. The final fractions of carbide-nitride phase in the equilibrium state are: IN718 – 0.32%, NbC – 0.91%, TiC – 1.12%, B_4C – 0.77%.

Based on the simulation results, the γ phase, NbC on TiN, Laves phases, and δ phase are the most likely to form during the solidification process. The possibility of σ and η phase formation cannot be excluded, as the experimentally obtained curve assumes a solidus temperature of approximately 1,100°C. However, their presence in the alloy is highly unlikely since the experimentally determined solidus temperature of IN718 ranges from 1,165°C to 1,230°C [38]. Additionally, many experimental studies performed on PBF-LB/M fabricated IN718 alloy [39,40] have not reported the presence of phases such as α-Cr, η, or τ. These differences between CALPHAD simulations and the experimental results are likely due to the approximations adopted in the models and the assumed cooling rates. For TiC and B_4C additions, both equilibrium and non-equilibrium

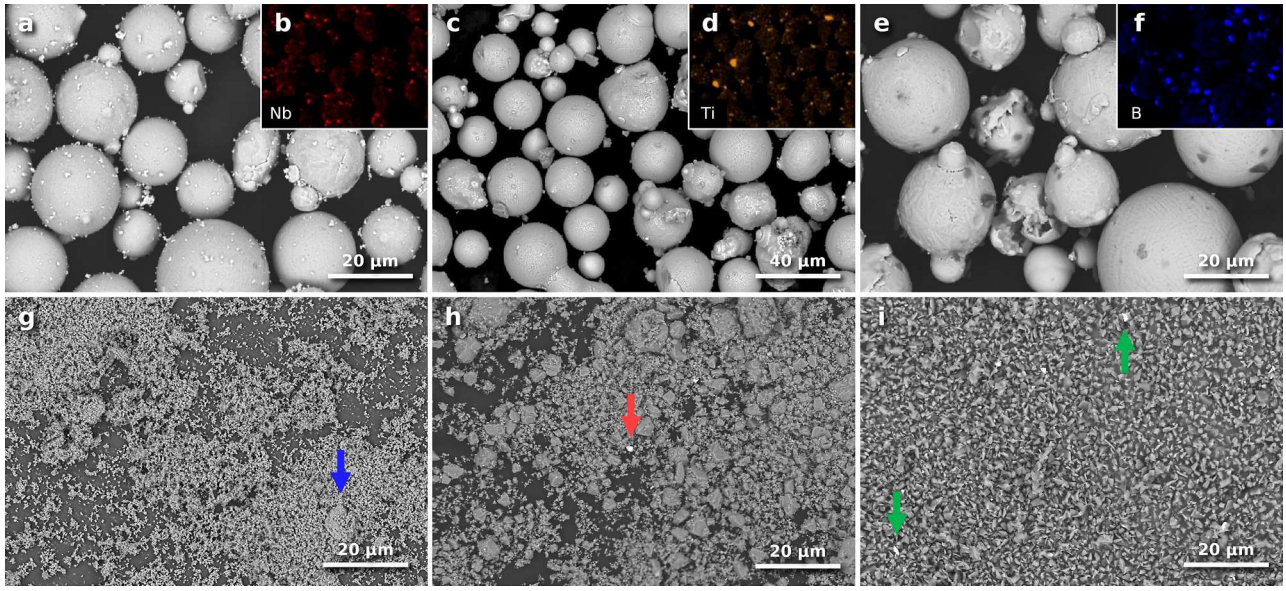

Figure 2. Micrographs of powders used in the study, SEM, BSE; (a) IN718-NbC; (c) IN718-TiC; (e) IN718-B_4C; Insets (b, d, f) – EDS maps showing base metallic element of the additive; (g) NbC; (h) TiC; (i) B_4C.

diagrams show more possible phases than those calculated for pure IN718 and IN718-NbC variants. In particular, the addition of B_4C can lead to the appearance of boron-containing phases such as (Mo, Cr, Fe)B_2 or TiB_2, as the compound introduces a new element (B) into the IN718 alloy. However, the main effect of the TiC and B_4C additions is the same as for NbC, a much higher proportion of carbide-nitride phases (NbC on TiN) and a higher liquidus temperature.

3.2. Properties of the powder mixtures

Figure 2 shows micrographs of IN718 powder enriched with carbide powders and base carbide powders. The morphology of the Inconel 718 powder is typical for gas atomised Inconel 718, with the majority of the particles being spherical. The carbide powders, although similar in nominal size (≈1–3 µm), show significant differences. The NbC powder is the finest, but a few oversized particles were found, as indicated by the blue arrow in Figure 2(g). The TiC powder does not meet the specifications. A significant volume of the powder particles is up to ≈20 µm in size. The TiC powder contains very few impurities identified by EDS, such as tungsten carbides (red arrow in Figure 2(h)). The B_4C powder is the most uniform of the three carbide-enriched powders, with particle sizes larger than those of NbC, but in accordance with the specification. No conglomerates or oversized particles were found. However, impurities in the form of oxides (Fe, Si) were found in the B_4C powder (green arrows in Figure 2(i)).

Figure 2(a–f) shows micrographs of IN718 modified with carbide powders. In the IN718-NbC powder, the additive particles are attached to the IN718 particles. The high niobium contrast allows the NbC particles to be easily distinguished in the SEM micrograph. Only the largest NbC particles can be clearly imaged due to the EDS sensitivity (Figure 2(b)). The IN718-NbC powder mixture shows the most uniform morphology. The larger PSD of TiC results in a more dispersed distribution with a larger average distance between the additive particles (Figure 2(c)). The uniformity of the IN718-B_4C powder mixture falls between that of the IN718-NbC and IN718-TiC powders. Both adherent and loosely dispersed B_4C particles are present in the micrographs (Figure 2(e)). However, the additive distribution is more uniform than that of IN718-TiC.

The effect of adding carbide powder to IN718 powder on the PSD of the mixed powders is noticeable, even with their small fraction (Figure 3(a)). TiC powder has the most significant influence, shifting the distribution curve toward lower particle sizes. This is because TiC particles are smaller in size than IN718 powder and do not adhere to IN718 particles. However, the PSDs of IN718-NbC and IN718-B_4C powders are almost identical to that of pure IN718 powder This confirms that the additive particles adhere primarily to the base powder surface and do not affect the PSD.

Figure 3(b) shows the diffuse reflectance of the mixed powders using a wavelength spectrum similar to that used in the PBF-LB/M machines (1060–1070 nm). All mixed powders show significantly reduced reflectance (2–4 pp), indicating higher light absorption by the carbide particles. IN718-TiC has the lowest reflectance, while IN718-B_4C has the highest. The decrease in reflectance and the differences are correlated with the volume percent of carbides added, with IN718-TiC having the highest percentage and IN718-B_4C having the lowest.

The presence of carbide particles has a negative effect on the flowability of all modified powders, as shown in Table 5. This is evident from the 25% higher Hall funnel flow times, lower bulk densities, and higher dynamic flowabilities expressed as mean flow angle and mean cohesion index. In contrast, the dynamic flowability of IN718-NbC powder is much less affected, with flow angle and cohesion index values nearly identical to those of pure IN718. Powders with less dense additives are more affected, and IN718-B_4C shows the highest average increase in the flow angle and cohesion index values.

The composition of base IN718 is in accordance with ASTM B637-18 (Table 6). The increase in carbon content slightly surpasses the specifications for carbide-modified powders, reaching 0.117 wt.% compared to the maximum allowable 0.08 wt.% for the highest carbon content in IN718-TiC. Carbide-forming metals show a significant increase. In the case of IN718-TiC powder, the Ti content increases from 1.08 wt.% to 2.53 wt.%. For IN718-NbC powder, the Nb content increases from 4.84 wt.% to 5.43 wt.%. Boron cannot be measured by the ED-XRF or combustion methods used. The expected weight percent of boron is calculated based on the measured carbon content in IN718-B_4C resulting in 0.162 wt.%.

3.3. PBF-LB/M fabrication

Figure 4 shows the porosity heatmaps of the as-fabricated samples, scaled to the maximum recorded porosity of 0.160% observed for the central set A, pure IN718 sample. The variance in energy density for set A ranges from 86% (101.6 J/mm^3) to 116% (137.3 J/mm^3) of the central point ED (117.9 J/mm^3), while for set B it ranges from 82% (109.8 J/mm^3) to 132% (176.8 J/mm^3) of the central point (117.9 J/mm^3). A total porosity of less

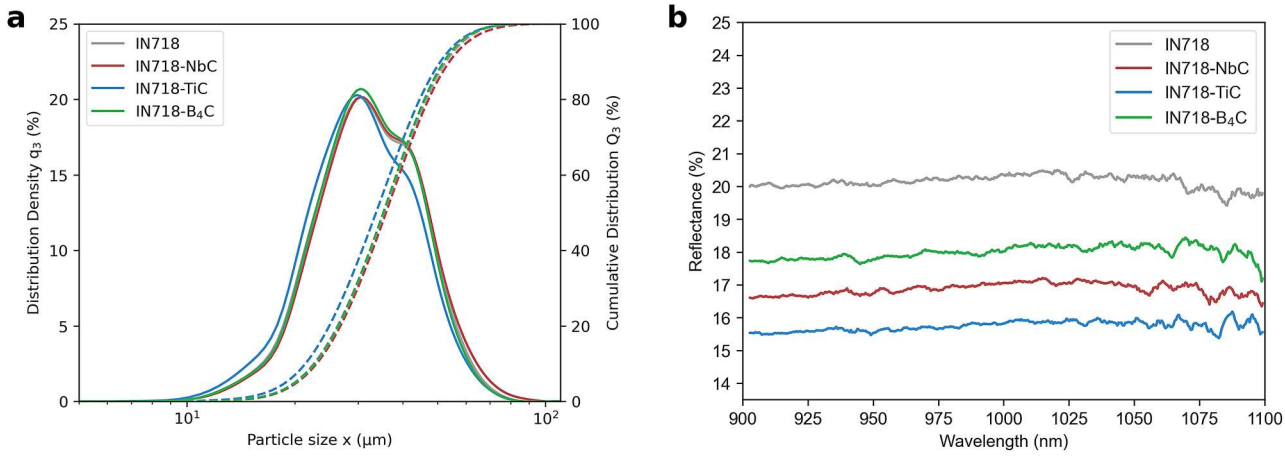

Figure 3. (a) Particle size distribution of carbide-modified IN718 powders; (b) Diffuse light reflectance of carbide-modified IN718 powders (smoothed).

than 0.1% was measured for most samples. IN718-B_4C has the lowest porosity with an average of 0.024%. In contrast, IN718 shows slightly higher levels of porosity, especially in set A, with an average of 0.068%, similar to IN718-NbC. IN718-TiC has the highest porosity with an average of 0.094%, but still remains below 0.1%. Faster scan speeds combined with smaller hatch spacing are beneficial for reducing porosity. The study found that changes in processing parameters within the parameter spaces of sets A and B did not significantly affect the porosity of reference IN718 or IN718-B_4C, indicating that both sets are within the acceptable processing window for all material variants. However, both IN718-TiC and IN718-NbC exhibit lower porosity at higher energy densities, suggesting that the parameter window can be expanded towards higher laser power and lower scan speeds.

Differences in porosity between samples, material variants, and parameter sets are very small and could be due to variations in the measurements in different sections. Similar to other studies [18], it was found that additives does not affect negatively the porosity of PBF-LB/M-processed IN718. The addition of B_4C may have a positive effect on porosity reduction during the PBF-LB/M process, despite the worse powder flowability (Table 5). This may be due to higher laser absorption (Figure 3(b)), as well as due to the fact that carbide particles may inhibit convection in the melt pool and alter the melting conditions [16].

Table 5. Flowability of carbide-modified IN718 powders.

Powder	Hall funnel flow time (s)	Bulk density mixture (g/cm^3)	Avg. flow angle (°)	Avg. cohesion index (-)
IN718	15.48 ± 0.16	4.73	43	11
IN718-NbC	21.08 ± 0.26	4.67	44.3	12.3
IN718-TiC	20.98 ± 0.27	4.68	48	14.2
IN718-B_4C	19.46 ± 0.20	4.57	50	15.5

Carbide powder particles may be lost during mixing [26], resulting in lower than expected C content. The expected weight of carbon was calculated by considering the mass of C in carbides (g/mol), the stoichiometric formula of the carbide, and its weight addition to the base IN718 powder. The results are shown in Table 7.

In pure IN718, the carbon content is 0.036% in the powder whereas 0.029% in the bulk material. Further carbide additions increase the powder carbon levels to 0.092% for NbC, 0.117% for TiC, and 0.076% for B_4C, with bulk samples containing slightly less. The observed carbon levels were below expectations, suggesting losses of carbide particles during mixing: 12.8% for IN718-NbC, 29.6% for IN718-TiC, and 6.1% for IN718-B_4C, resulting in actual additions of 0.49 wt.% NbC, 0.38 wt.% TiC, and 0.18% wt.% B_4C.

Additive powder properties have a significant effect on carbon loss during powder mixing, especially with large differences in weight ratios (more than 100:1) and particle sizes (15–45 µm vs. ≈1 µm). Factors such as carbide particle adhesion, density, and the presence of oversized particles influence these losses, as evidenced by residues on mixing equipment and sieve screens. The variation in carbon loss is correlated with the uniformity of the carbide powder: B_4C had the lowest loss and the highest uniformity, NbC had moderate levels of both and TiC, with irregular particles and conglomerates, had the highest loss of nearly 30%. Comparatively, the present investigations showed less carbide addition loss than Markanday et al. [26], who reported only a quarter of the intended NbC addition with 5–10 µm powders. In conclusion, refined mixing

Table 6. Chemical composition of powders used in the study measured by combustion (for C) and ED-XRF (for other elements) methods (error as SD from 3 separate measurements).

Element	IN718[a] (wt.%)			IN718 (wt.%)	IN718-NbC (wt.%)	IN718-TiC (wt.%)	IN718-B_4C (wt.%)
	Min	Max	Avg.				
Ni	50	55	52.5	54.04 ± 1.05	53.78 ± 2.29	52.87 ± 1.24	55.09 ± 1.55
Cr	17	21	19	17.29 ± 0.60	17.23 ± 2.08	17.15 ± 0.35	15.88 ± 0.43
Fe	11.1	24.6	17.85	17.46 ± 0.1	17.30 ± 0.15	17.21 ± 0.15	17.86 ± 0.21
Nb	4.8	5.5	5.15	4.84 ± 0.25	5.43 ± 0.25	4.74 ± 0.28	4.98 ± 0.31
Mo	2.8	3.3	3.05	2.95 ± 0.16	2.95 ± 0.17	2.88 ± 0.15	3.05 ± 0.24
Ti	0.65	1.15	0.9	1.08 ± 0.02	1.07 ± 0.09	2.53 ± 0.09	1.88 ± 0.11
Co	0	1	0.5	0.09 ± 0.01	0.09 ± 0.02	0.09 ± 0.02	0.08 ± 0.02
Al	0.2	0.8	0.5	0.603 ± 0.09	0.677 ± 0.008	0.697 ± 0.007	0.56 ± 0.008
Mn	0	0.35	0.175	0.002 ± 0.001	0.002 ± 0.001	0.002 ± 0.001	0.002 ± 0.001
Si	0	0.35	0.175	0.05 ± 0.03	0.04 ± 0.03	0.09 ± 0.06	0.07 ± 0.05
N	0	0.10	n/a	0.013[b]	Not measured	Not measured	Not measured
C	0	0.08	0.04	0.036 ± 0.003	0.092 ± 0.017	0.117 ± 0.004	0.081 ± 0.012
B	0	0.006	0.003	Not measured	Not measured	Not measured	0.162 (calc.[c])
Ta	Max 5.5 – Nb			0.323 ± 0.023	0.375 ± 0.033	0.331 ± 0.022	0.304 ± 0.023

[a]ASTM B637-18 standard; [b]Measured by high-temperature extraction method – the same IN718 powder is used as in [33]; [c]Calculated based on C content in B_4C and C measured by combustion method (Table 7).

procedures to account for potential losses are recommended for all studies involving powder mixtures.

3.4. As-built microstructure

The microstructure of PBF-LB/M fabricated IN718 has been the subject of numerous studies [39,41–43]. Both NbC and TiC carbides are typically found in PBF-LB/M-ed IN718 [32], especially after HT. The four materials in as-built (AB) condition (Figure 5) are characterised by a typical IN718 PBF-LB/M microstructure. In BD (Figure 5 (c, e, and g)), columnar γ-grains elongated in the direction of build are cross sectioned with solute banding lines, i.e. laser track interfaces outlined during the PBF-LB/M process by subsequent layer-by-layer laser melting. A study by Chang et al. showed that NbC additions can change the average melt pool depth with a significant decrease from 223.4 µm with 0% NbC to 139.4 µm with 5.0% NbC [16]. However, the present results show that small additions do not affect the morphology of the melt pool. Micrographs in the in-plane direction (IPD) show the regular arrangement of solute-rich bands of individual tracks according to the applied scanning strategy, i.e. zig-zag checkerboard strategy, rotated by 90° and shifted by 50% in each layer (Figure 5(b, d, f, and h)).

Arrays of parallel dendritic cells within columnar grains are observed within columnar γ-phase grains of PBF-LB/M-ed IN718. This substructure consists of packets of parallel dendritic cells with small misorientation angles ($2° < \theta < 5°$), where each packet is separated by low-angle grain boundaries ($5° < \theta < 15°$) inside larger grains [3]. It also creates a high density dislocation network as discussed in [44,45]. Micrographs in the build direction (BD) show similar arrangements of cellular dendrites in all material variants. However, the IPD micrographs show differences. In reference IN718, dendritic cells are cross sectioned perpendicular to the direction of growth, indicating BD directional growth regardless of location. However, for all modified variants in IPD, dendritic cells in the vicinity of the laser track interfaces show a similar morphology as in the BD cross section (marked with yellow arrows in Figure 5(d, f, and h)), indicating that the growth direction in these regions has been modified by the addition of carbides.

All material variants show periodically spaced, much deeper melt pool marks (marked by black arrows in Figure 5(a, c, e, and g)). The spacing of these deeper melt pool marks corresponds to the spacing of the checkerboard squares and are identified as scarfs after the start of scanning of individual checkerboard squares. These regions must have had a much higher laser energy input and temperature gradient, resulting in a tendency for cellular growth.

The built micrographs also reveal the presence of oversized carbides, which are found in higher amounts in IN718-TiC and in lower amounts in IN718-NbC (indicated by magenta arrows in Figure 5(c–f)). The carbides are randomly distributed and do not show any tendency to conglomerate. The size and distribution density of the oversized carbides are consistent with the powder characteristics of the carbide powders (Figure 2). Micrographs suggest that the laser melting parameters used do not provide sufficient energy to melt oversized carbides. The melting temperature of B_4C is 2,350°C, while for TiC and NbC it is 3,160°C and 3,490°C, respectively. PBF-LB/M melt pool simulations for IN718 suggest that the melt pool temperature in its centre can reach 3,000°C [46,47], thereby verifying the inability to dissolve the largest TiC and NbC carbides. Large carbides are not visible in the IN718-B_4C micrographs, however, cracks are found within the micrographs, as marked by the

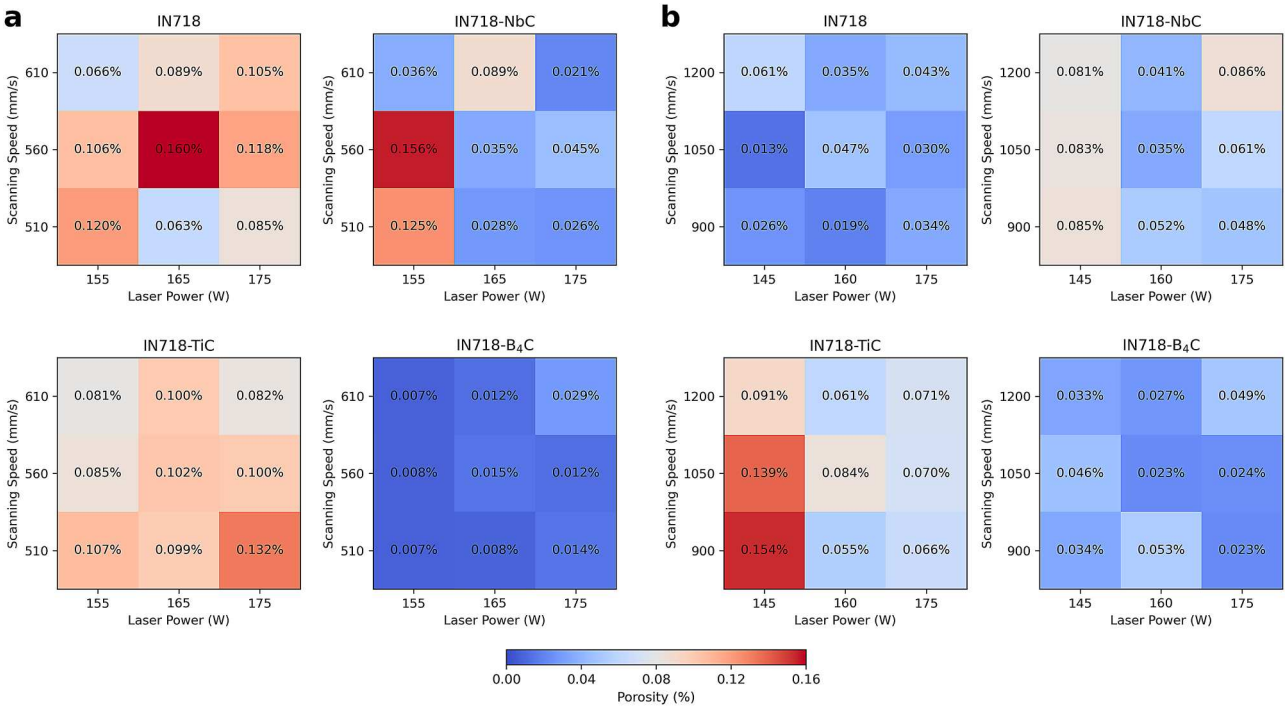

Figure 4. Porosity in relation to scanning speed, laser power, and material variant; (a) set A; (b) set B.

blue arrow (Figure 5(g)). The cause of which can be associated with a significant addition of boron and will be discussed later.

Hsu et al. also found that large additive flakes did not decompose during the PBF-LB/M process, while particles below 3–5 µm were possible to melt [15]. Large particles are highly undesirable, but large individual particles are much less harmful than small flakes, which can have multiple internal boundaries and can act as crack initiation points, reducing material ductility [16]. In contrast, nanoscale additives tend to agglomerate due to their strong Van der Waals forces [28]. Their dispersion during PBF-LB/M solidification is sensitive to the laser energy per unit length. Depending on the processing parameters chosen, the distribution of added nanoparticles within the alloy can range from severe aggregation to uniform dispersion [29].

The formation of Laves phases and carbides along intercellular boundaries in PBF-LB/M processed IN718 is primarily driven by solidification behaviour characterised by cell dendritic growth and microsegregation of elements such as Nb, Ti and Mo. These phenomena are significantly affected by PBF-LB/M processing parameters, including laser power and scanning speed [3,48], which influence non-equilibrium eutectic transformations. Figure 6(a–d) demonstrates, that the carbide addition does not influence the cell spacing and morphology of the intercellular boundaries, but are mainly defined by the chosen PBF-LB/M process parameters (Table 2). In contrast, Gu et al. found that columnar dendrites were enhanced and the dendrites spacing of γ was decreased by the higher additions of TiC, however at higher concentrations, i.e. 10 wt.% TiC [28].

While the Laves phase and NbC are present after solidification in cast IN718 [49,50], NbC is not formed extensively during the PBF-LB/M process due to the high cooling rate and suppression of NbC precipitation by solute trapping [51], similar to sub-rapid casting [49]. DuPont et al. [31] also showed that addition of NbC can result in a decreased volume fraction of the Laves phase on solidification for IN718-NbC compared to IN718. Interestingly, the addition of carbides also does not appear to significantly affect the presence of globular precipitates. Exemplary morphology is shown at higher magnification in Figure 6(e–f) for the IN718-TiC variant. This may be explained by the CALPHAD simulation result (Figure 1(c)), which indicates that at the beginning of the solidification process, these precipitates are mainly composed of Ti and N. Therefore, nucleation is driven by the presence of nitrogen in the alloy (0.013 wt.%, see Table 6). Here, the nitrogen content should be similar for all variants since the mixed powders and reference powder were prepared from the same batch of IN718. Toward the end of the solidification process, Nb and C become the main elements in the phase. The size of the particles is <50 nm, so these are not carbides added by powder

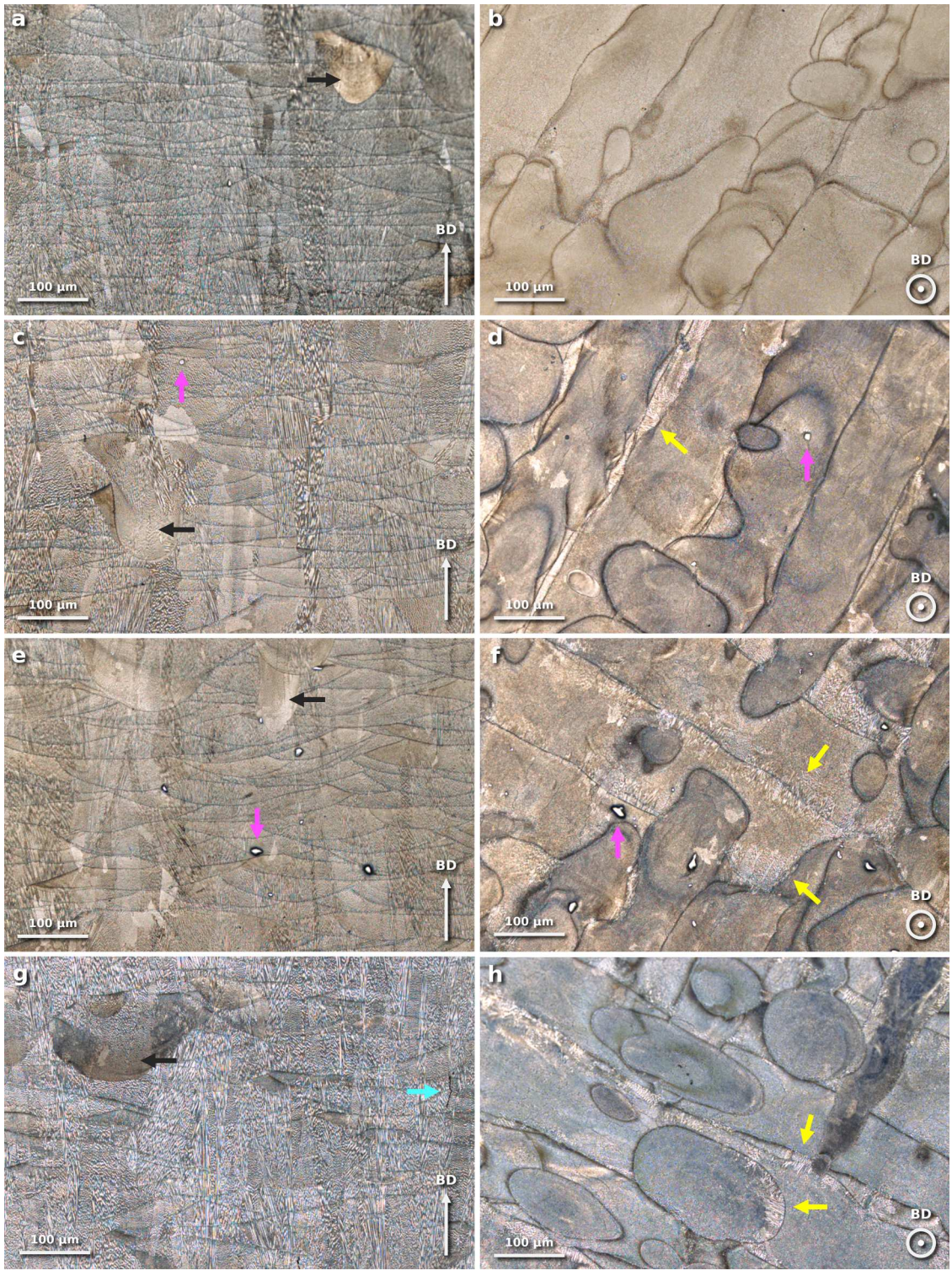

Figure 5. Micrographs of carbide-modified IN718, as-built (AB) in the build direction (a, c, e, g) and in-plane direction (b, d, f, h), etched with Glyceregia, OM; (a, b) IN718; (c, d) IN718-NbC; (e, f) IN718-TiC; (g, h) IN718-B_4C.

mixing (1–3 µm), but two-phase particles in the form of NbC on TiN as suggested by CALPHAD. The size of carbide-nitride particles and the absence of carbide particles in the added sizes (≈1–3 µm) confirm that most of the added carbide particles dissolved during the PBF-LB/M processing and reprecipitated as carbide-nitrides during solidification.

Similar results were presented for Inconel 625 welds [52], where the authors observed by transmission electron microscopy (TEM) analysis that precipitates in the

Table 7. Carbon content in powder and bulk PBF-LB/M samples measured by combustion method (error as SD of 3 measurements).

Sample	Molar mass of additive (g/mol)	Additive fraction (wt.%)	Expected carbon content in sample (wt.%)	Carbon measured in powder sample (wt.%)	Carbon measured in the PBF-LB/M sample (wt.%)	Carbon loss* (%)	Adjusted additive fraction** (wt.%)
IN718	n/a	n/a	n/a	0.036 ± 0.003	0.029 ± 0.001	n/a	n/a
IN718-NbC	92.9	0.6	0.0975	0.092 ± 0.017	0.085 ± 0.002	12.8%	0.49
IN718-TiC	47.9	0.6	0.1492	0.117 ± 0.004	0.105 ± 0.004	29.6%	0.38
IN718-B_4C	10.8	0.2	0.0724	0.076 ± 0.001	0.068 ± 0.003	6.1%	0.18

*The percentage decrease in carbon content expected to measure, in the PBF-LB/M sample.; **The recalculated weight percentage of the carbide additive based on the measured carbon content.

IN625 weld, typically assumed to be NbC carbides, are actually carbide nitrides with a core rich in Ti and N. The authors state that, despite significant variations in composition, no significant change in the crystallographic form of the precipitates was found. The mechanism of nitride formation was discussed by Lim et al. [53] for laser-based direct energy deposited (L-DED) Inconel 718. Since L-DED operates under coaxial argon gas, it cannot entirely prevent air exposure, introducing nitrogen into the melt pool in amounts exceeding its solubility in a nickel-based superalloy ($\approx 2.9 \cdot 10^{-3}$–$6.2 \cdot 10^{-2}$ wt.% at 1327–1727°C). During solidification, titanium in IN718 segregates into the liquid phase and moves to the surface of the melt pool, forming TiN due to its strong affinity for nitrogen [54]. Given that TiN has a much higher melting temperature (2,930°C) compared to IN718 (solidus ranges from 1,165°C to 1,230°C [38]), TiN nucleates and grows while the alloy matrix remains liquid. Carbide nitrides were also identified in another study in which TiC was added to IN718 processed by PBF-LB/M and the presence of Ti, Nb, N and C in the precipitates was confirmed [37]. Similar findings were observed in Wire Arc Additively Manufactured (WAAM) IN718 [55].

The above discussion leads to a conclusion that the formation of carbonitrides is primarily driven by the presence of nitrogen in quantities exceeding its solubility – 0.013 wt.% in this study compared to the referenced 0.0029 wt.% at 1,327°C – rather than by the dissolution of micron-sized TiC particles added via powder mixing. Although the increased Ti fraction from the dissolved TiC addition is significant, our results show that the formation of carbide-nitrides begins in the liquid phase and is followed by NbC precipitation. This is further supported by the significant presence of carbide-nitrides in both pure IN718 and IN718 modified with NbC or B_4C.

Figures 7 and 8 show EBSD results of as-built materials, indicating that carbide addition does not significantly affect the texture of the AB alloy. All variants are characterised by elongated grains, with an average grain size by number ranging from 23 to 26 µm. The addition of carbides slightly influences grain morphology, introducing a few larger grains, which increases the average grain size by area fraction from ≈100 µm for IN718 to ≈ 200 µm for IN718-NbC and decreases the average aspect ratio from 0.12 for IN718 to 0.17 for IN718-TiC (Figure 8). All materials exhibit a strong Goss texture component {110} < 001>, as seen in the pole figures in Figure 7(c, d, g, and h), where the <001 > direction is parallel to the building direction and the {110} plane family. The peak pole density is similar for all materials, ranging from 11.76 for IN718 to 12.79 for IN718-NbC.

The GB misorientation angle (Figure 8(a, d, e, and j)) is also slightly affected by carbide addition. All materials have a high proportion of very low angle grain boundaries (VLAGBs; $\theta < 5°$), ranging from more than 60% of all GBs for IN718 to 45% for IN718-B_4C. A high number of VLAGBs can be associated with long, epitaxially grown grains, limiting the fraction of other boundary types due to the lower length of the GB compared to equiaxed grains. The overall texture evolution during PBF solidification is controlled by the processing parameters such as layer height, hatch distance, energy density, or scanning strategy. In this study, the parameters used included low layer height and scan speed, accompanied by a relatively large hatch distance (see Table 2), and high laser power relative to focus diameter. Such a combination of parameters results in a wide and shallow melt pool, which is typical for highly textured IN718 [40,56,57]. Other studies show that e.g. NbC particles can enhance texture by restricting growth along certain directions [26]. In this study, possibly due to low carbide addition, the as-built texture of IN718 is only slightly influenced, regardless of the type of carbide added.

3.5. Heat-treated microstructure

The study aims to develop a method for controlling grain structure in IN718 alloy after PBF-LB/M processing and subsequent hot isostatic pressing. Previous studies suggest that the chosen holding time and temperature of the stress relief process (1,150°C/6 h)

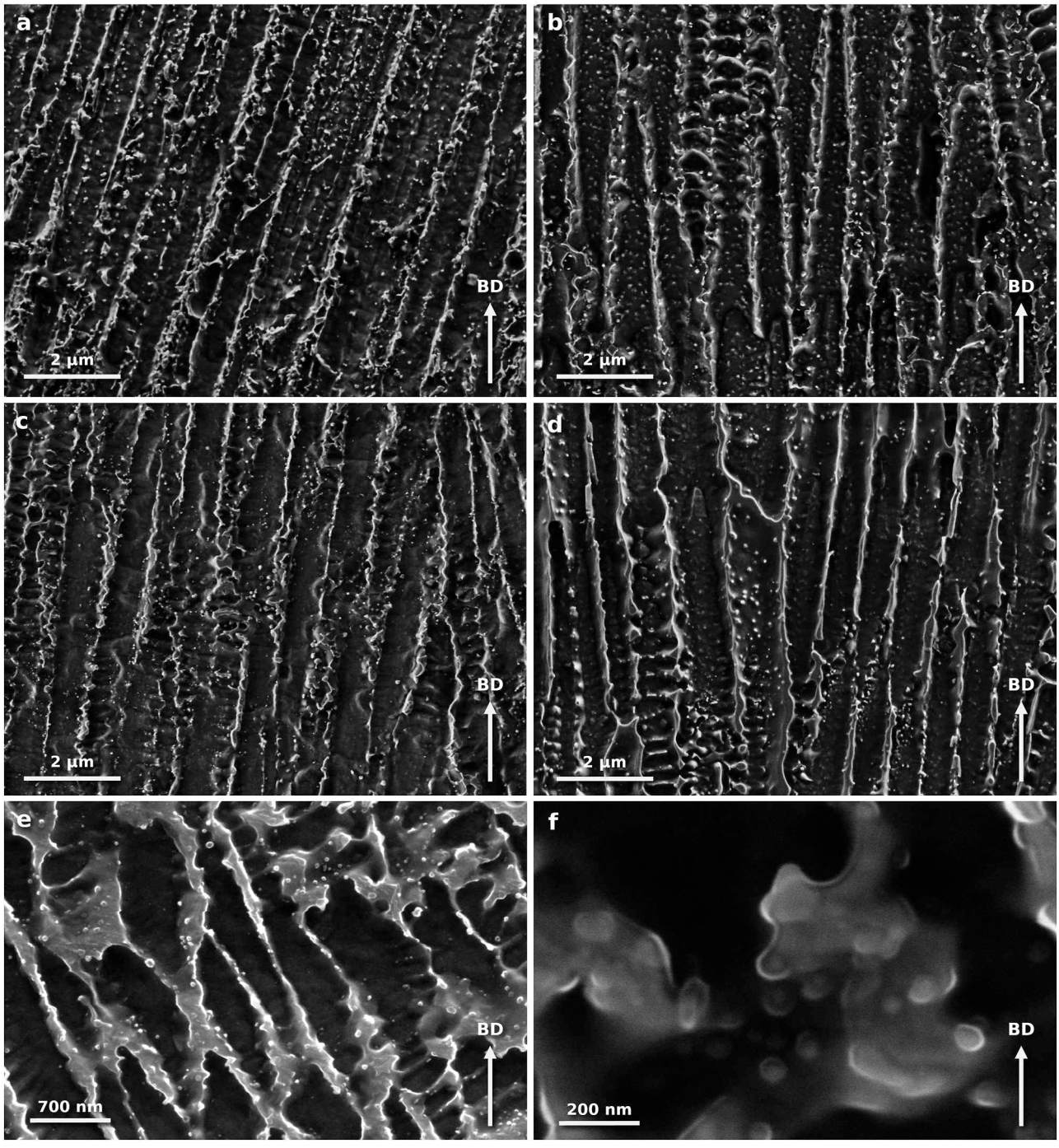

Figure 6. Micrographs of carbide-modified IN718, as-built (AB), cross-section parallel to the building direction (BD), etched with Glyceregia, SEM, SE; (a) IN718; (b) IN718-NbC; (c) IN718-TiC; (d) IN718-B_4C.; (e, f) morphology of NbC on TiN carbide precipitates – IN718-TiC sample.

should be sufficient to result in homogenisation of PBF-LB/M-ed IN718, removal of low angle grain boundaries, removal of dendritic cell substructure, and removal of all secondary phases except (Nb, Ti)C primary carbides [3,32]. At the same time, PBF-LB/M-ed IN718 is characterised by non-deformed high angle grain boundaries (HAGB) of the γ-phase compared to forged IN718. The PBF-LB/M-ed alloy, with its energy reduced by solute atoms and HAGBs pinned by undissolved carbides, results in HAGBs that migrate much more slowly than the deformation-induced HAGBs of the cold-worked material. As expected, pure IN718 shows the above after stress relief treatment (Figure 9). The stress relief process is aided by the twinning observed in the BD and IPD micrographs of pure IN718.

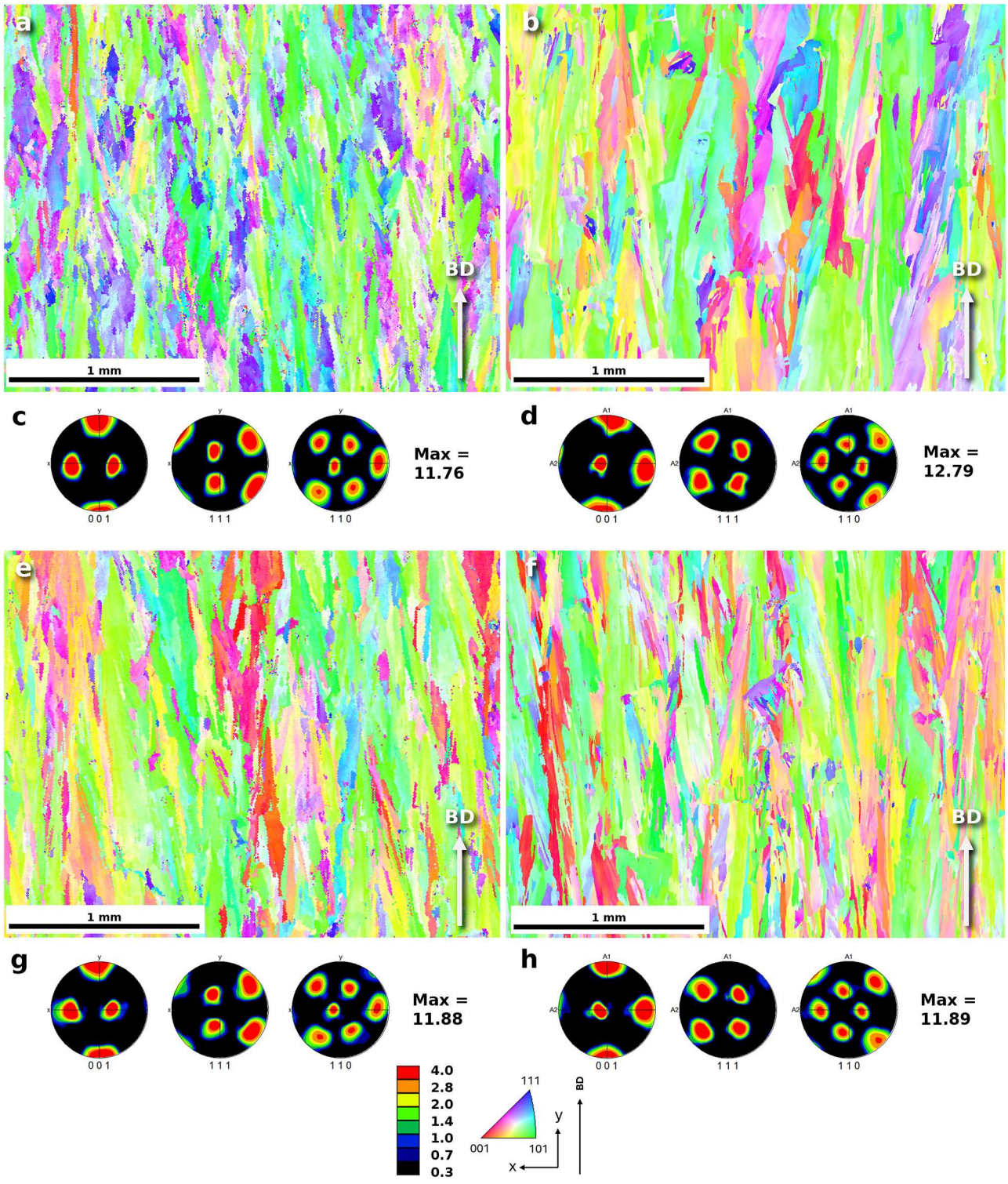

Figure 7. Inverse pole figure maps with colouring in the out-of-plane direction and corresponding pole figures for IN718 (a, c), IN718-NbC (b, d), IN718-TiC (e, g) and IN718-B_4C (f, h) in as-built condition.

Significant differences are observed for the heat-treated carbide-modified material variants. Each carbide-enriched IN718 shows a different degree of homogenisation. IN718-NbC is the most homogenised, with almost complete removal of the dendritic cell substructure. However, compared to pure IN718, the majority of LAGBs are still present. IN718-TiC and IN718-B_4C show similar general microstructures. LAGBs are preserved, and traces of former dendritic cells are still clearly visible.

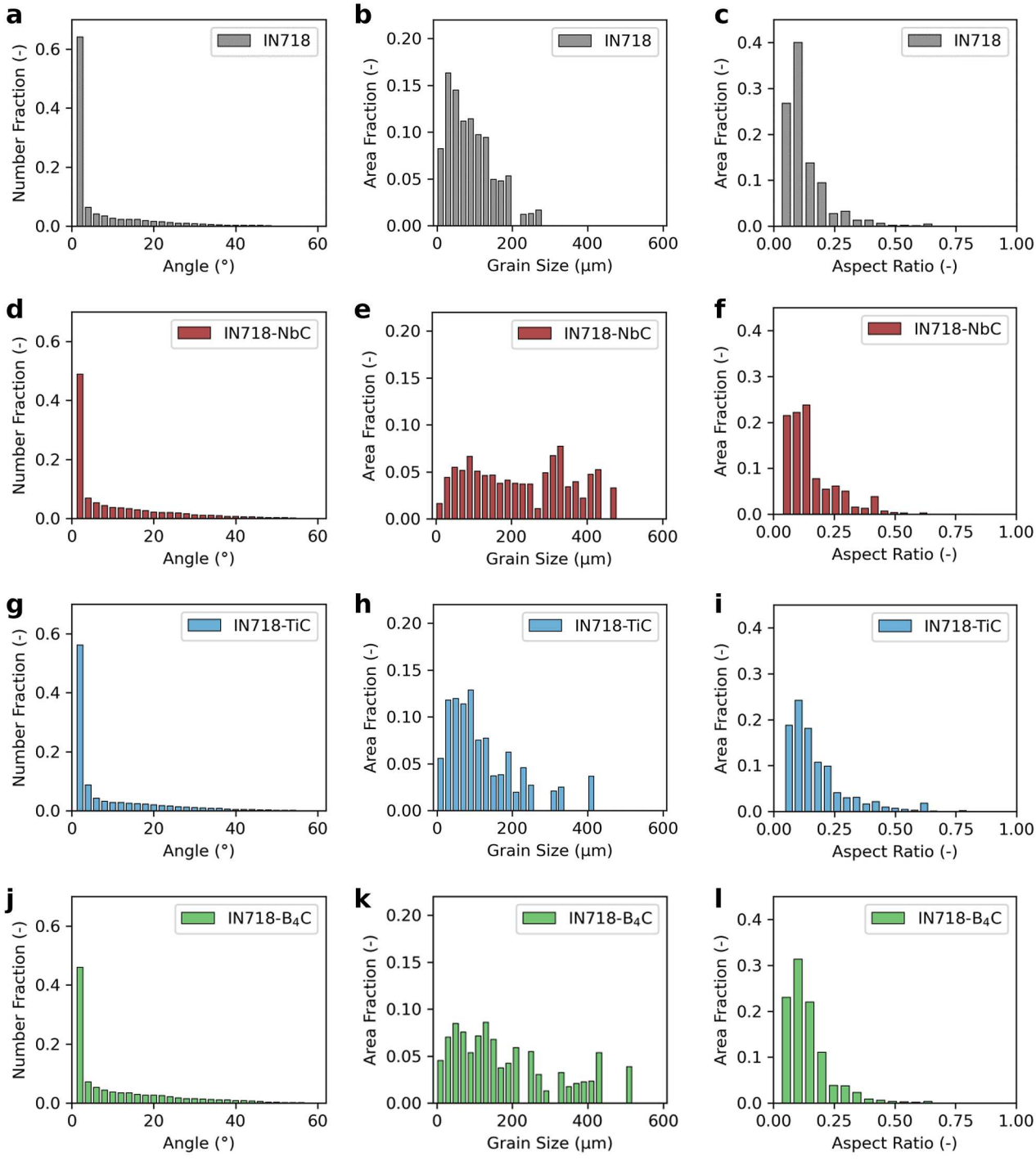

Figure 8. Bar plots of misorientation angle (a, d, g, j), grain aspect ratio (b, e, h, k), and grain size (c, f, i, l) for IN718 (a–c), IN718-NbC (d–f), IN718-TiC (d–f), and IN718-B_4C (d–f) in as-built condition.

Examination of AB samples showed that most of the added carbides were melted during the PBF-LB/M process. In addition, carbon is known to segregate at the GB in nickel superalloys [58]. Previous studies suggest that modified particles should be distributed mainly along the GB due to the pushing effect of the particles by the solidification front [30]. However, with decreasing size, the particles are expected to be captured by the solidification front and distributed within the grains, as their moving velocity is lower than the solidification rate considering their nanoscale dimensions [28].

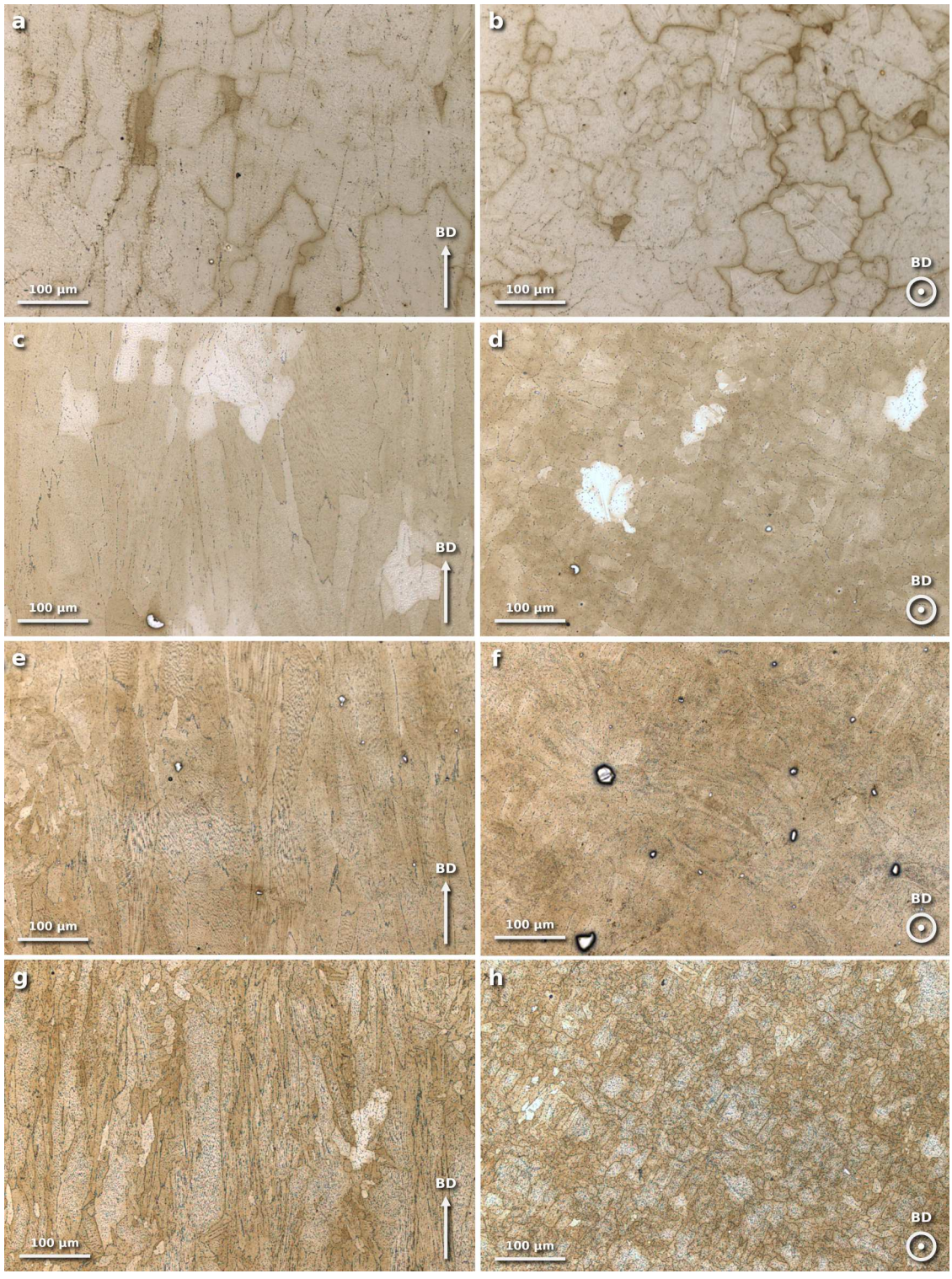

Figure 9. Micrographs of carbide-modified IN718, stress relieved (SR) in the build direction (a, c, e, g) and in-plane direction (b, d, f, h), etched with Glyceregia, OM; (a, b) IN718; (c, d) IN718-NbC; (e, f) IN718-TiC; (g, h) IN718-B_4C.

SEM micrographs (Figure 10) for IN718-NbC and IN718-TiC show that segregation occurs not only at GBs, but also in the interdendritic regions. Increasing the homogenisation temperature results in faster kinetics of NbC formation [51], and high diffusion of both C and Nb atoms in the Ni matrix, which drives NbC carbide formation [59]. Figure 10(b and c) show that carbides are formed at all types of GBs, from VLAGBs between dendritic cells, over LAGBs between dendritic cell bundles, to HAGBs. The smallest carbides are

formed at VLAGBs and the largest at HAGBs. It is easy to distinguish between newly formed and added carbides, as they are characterised by round edges, probably due to partial surface melting, and a visible difference in SEM contrast, indicating a higher level of elements with a lower atomic number (Ti in Figure 10(d)).

Figure 10(e) shows a subcellular crack in the B_4C sample. As mentioned, a small number of similar cracks were found during the OM observations. Mandal et al. [23] also observed micro-cracks in the metal matrix composite of IN718 and B_4C prepared by PBF-LB/M. The study discussed that at the interface between B_4C particles and IN718 matrix, the average von Mises stresses are 2 times higher than between TiC and IN718. This resulted in a higher stress concentration and microcrack formation. EDS studies showed no change in chemical composition in the crack region compared to the bulk of the alloy. It is also important to note that there were no cracks after HIP, indicating that the applied HIP densification is sufficient for small crack healing in IN718-B_4C.

Figure 11 shows the size distribution of carbides for different material variants. After HT, pure IN718, IN718-NbC and IN718-TiC show similar average sizes, with equivalent dia. of 0.13 µm for pure IN718 and 0.17 µm for both IN718-TiC and IN718-NbC, while IN718-B_4C shows significantly larger sizes with an average of 0.32 µm. IN718-TiC stands out in the carbide distribution compared to other variants, with a high density of small carbides. This can also be observed by comparing the micrographs in Figure 10. According to Table 7, the carbon content in the bulk samples is 0.029 wt.% for IN718, 0.085 wt.% for IN718-NbC, 0.105 wt.% for IN718-TiC and 0.068 wt.% for IN718-B_4C.

The correlation between the average area occupied by carbides and the measured carbide content is consistent for IN718, IN718-NbC and IN718-TiC (Figure 11(e and f)). However, the area occupied by precipitates is the largest for IN718-B_4C (2.29%) despite having the second lowest carbon addition. Both Nb and Ti are standard alloying elements of IN718 (see Table 6), so atypical precipitates are not expected with increasing Ti and Nb contents. However, the B content in pure IN718 does not exceed 0.006 wt.%, while in the IN718-B_4C alloy B is increased to ≈0.16 wt.%, suggesting that the chemical composition of the precipitates in IN718-B_4C must be different from those of the other variants of materials. This is also suggested by CALPHAD simulation, as the area fraction occupied by the precipitates is slightly lower than the carbide-nitride phase determined with the equilibrium diagram for non-boron variants. The differences are as follows: IN718 – 0.09 pp, IN718-NbC – 0.22 pp, IN718-TiC – 0.02 pp, while for IN718-B_4C, the difference is much higher at 1.52 pp. Equilibrium state simulation refers to ideal conditions, where carbides are completely dissolved, and the liquid phase is characterised by a uniform distribution of elements throughout its volume, so slightly higher simulated concentrations are expected.

Based on the EDS scans (Figure 12), the chemical composition of the precipitates is similar for IN718, IN718-TiC and IN718-NbC. Despite the increased Ti content in IN718-TiC, the main carbide-forming element is Nb. In addition, a significant intensity of Mo is registered, as well as a less pronounced signal from Ti and C. Non-melted carbides in the IN718-TiC sample are clearly distinguishable from other precipitates (Figure 12(e)). This is confirmed by the EDS line scan in Figure 12(f), as the particle is mainly composed of Ti and C.

With the addition of B_4C the chemical composition of the precipitates show an increased signal of Mo, even exceeding Nb. Other elements such as Ti, C and B are also detected. In addition, the intensities of Cr and Fe in IN718, IN718-NbC and IN718-TiC follow the intensity of Ni, while in IN718-B_4C the intensities of Cr and Fe decrease but do not follow the intensity of the matrix (Ni-Cr-Fe). Due to the fact, that boron is a very low energy and the line of boron overlaps with the lines of niobium and molybdenum (0.182, 0.172 and 0.193 keV respectively) detecting boron peak in the EDS spectra is challenging [60]. However, borides can be identified using EDS by focusing on the main boride-forming elements, and by comparison to carbides formed other in boron free variants. CALPHAD simulations suggest (Figures S1d and S2d) that the addition of B_4C may lead to the precipitation of diboride phases such as TiB_2 or (Mo, Cr, Fe)B_2. EDS results suggest the latter. Similar results were found by Tekoğlu et al. who found that ZrB_2 decomposed into (Zr, Ni)-based intermetallic and (Nb, Mo, Cr)-based boride during PBF-LB/M processing of IN718 + ZrB_2 mixture [18].

Borides can precipitate at grain boundaries when IN718 is heated subsolvus δ (above 1050°C) even with low boron content (0.0037–0.0039 wt.%), as demonstrated by Vernier et al. [60]. They identified (Nb, Mo, Cr)$_3B_2$ borides in cast-and-wrought IN718 using TEM-EDS. Borides are also suggested to help control the alloy grain size through grain boundary pinning, similar to carbides. Kontis et al. [61] found by atom probe tomography (APT) that in boron-containing superalloys, borides are more common than carbides at the grain boundaries and significantly affect mechanical properties. In a medium-boron alloy, serrated grain boundaries were observed, which improved creep properties. However, if the volume fraction of borides exceeded a threshold of 0.05 at.% (0.00315 wt.%), the

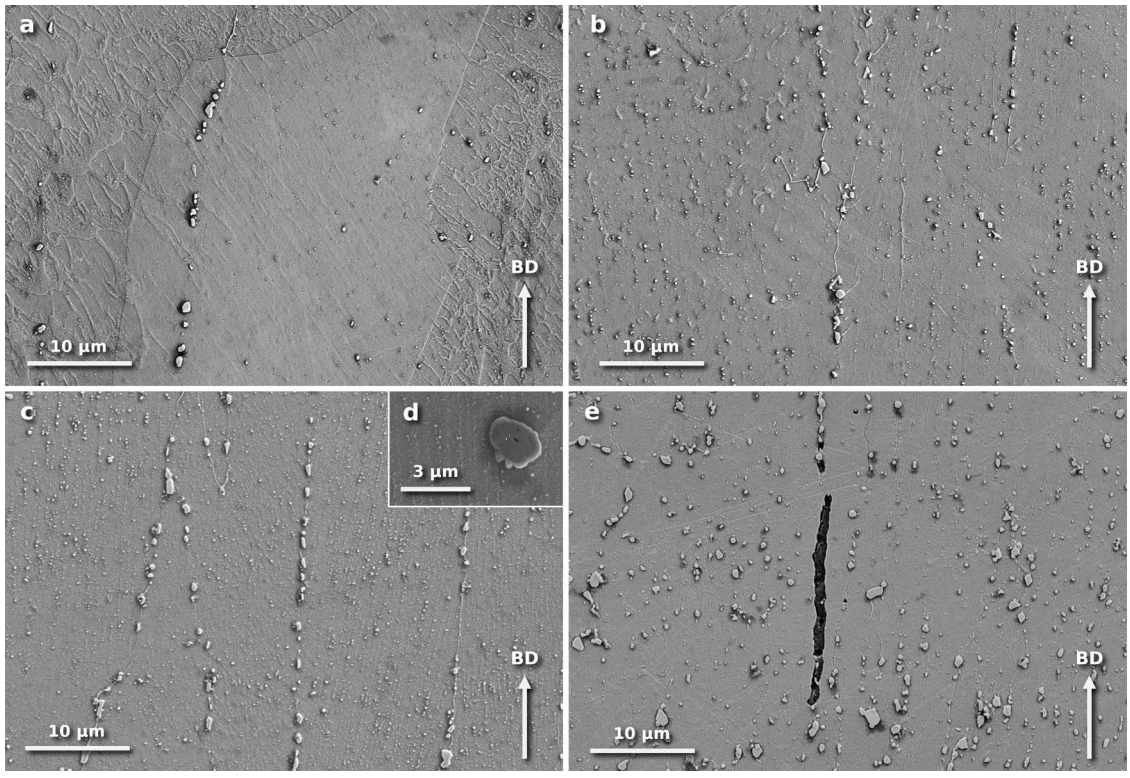

Figure 10. Micrographs of carbide-modified IN718 after stress relief annealing (SR), cross-section parallel to the building direction (BD), etched with Glyceregia, SEM, SE; (a) IN718; (b) IN718-NbC; (c) IN718-TiC; (d) partially melted, oversized TiC particle; (e) IN718-B_4C.

creep properties begin to decline. This threshold is much lower than the B content in IN718-B_4C (0.162 wt.%), but in the cited study, borides precipitated exclusively at the grain boundaries, resulting in nearly continuous boride formation. In our study, borides and carbides are distributed more evenly, suggesting a higher B content threshold.

Figures 13 and 14 show the EBSD results of fully heat-treated materials. Significant differences can be seen between all variants. High pressures, temperatures, and long holding times during HIP result in homogenisation and significant grain growth in pure IN718, accompanied by annealing twinning, identified as the main process supporting the recrystallization of PBF-LB/M prepared IN718 [3]. Twin boundaries, characterised by a 60° misorientation, state for 40% of all GBs (Figure 14). Compared to the AB state, pure IN718 texture after HT is significantly reduced (peak pole density decreased from >11 to <5). Random texture with Goss texture residues can still be observed (Figure 13(a and b)). A similar homogenisation characteristic is observed for IN718-NbC. Here, the texture is even lower (peak pole density is 3.53) and the twin boundary fraction is ≈45% (Figure 14(d)). However, for both material variants, recrystallization has not yet been fully achieved, as indicated by the remaining ≈20% fraction of VLAGBs (Figure 14(a and d)). The average aspect ratio for IN718 and IN718-NbC is similar, i.e. 0.30 and 0.33, therefore the grain aspect ratio is 2 times lower than in the case of the AB counterparts. The main difference between IN718 and IN718-NbC is the grain size. IN718 is characterised by very large grains, with an average grain size by area fraction of 209 µm, whereas IN718-NbC grains are smaller, with an average grain size by area fraction of 110 µm (Figure 14 (b and e)). This effect has been widely observed in the literature, and the increased volume fraction of carbides contributes to the enhancement of the Zener pinning effect, resulting in smaller grain sizes after heat treatment for carbide-modified IN718 [15–17,28].

Comparison of as-built IN718-TiC and heat-treated IN718-TiC shows that TiC addition resulted in almost complete suppression of the recrystallization (Figures 7 (b) and 13(e)). The HT variant shows as high-level Goss texture, with a peak pole density of 12.84, same as the AB variant, while 60° twin boundaries are almost absent. Additionally, the average aspect ratio and grain size by area fraction for HT IN718-TiC are 0.16 and 91 µm, respectively. These are almost identical to the AB averages. However, the proportion of VLAGBs has decreased from 60% to 50% (Figures 8 and 14(g)). This indicates that minimal homogenisation has occurred. Due to the much enhanced pinning effect caused by

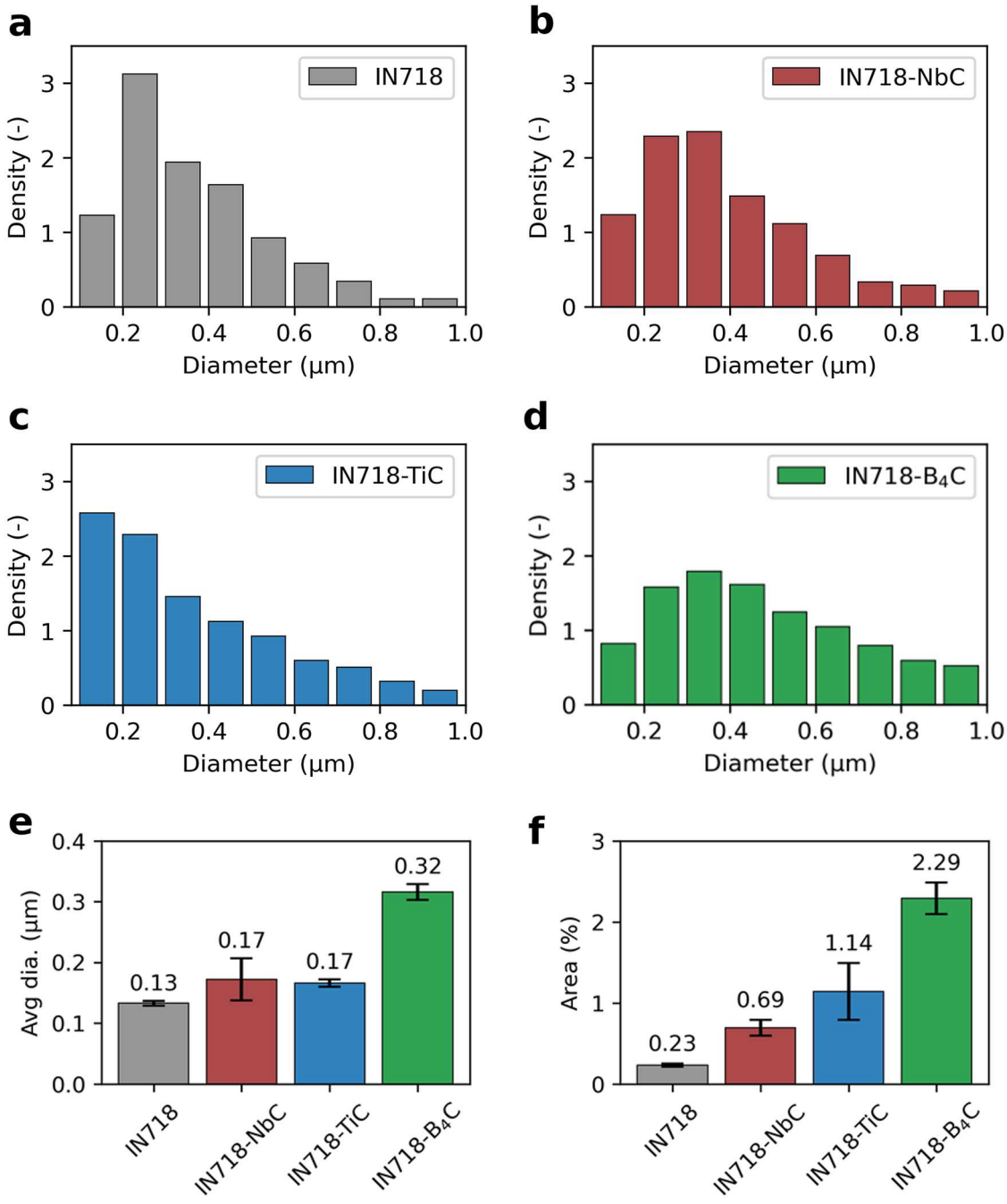

Figure 11. Histograms showing carbides size distribution in relation to material variant (a–d); average carbide diameter (e); and occupied area (f). Error bars – std deviation; average values above the bars.

the discussed differences between IN718-NbC and IN718-TiC (see Figures 10 and 11), the pinning effect acts not only at HAGBs, but down to the level of dendritic cells, surpassing recrystallization even during HIP. The role of small carbide precipitates in preserving the as-built texture is evident from a comparison with IN718-B_4C (Figure 13(f and h)). The observed number and size of precipitates were highest for IN718-B_4C (Figure 11), but their effect on the recrystallization of IN718 is lower. There is visible grain growth at the edges of the IPF map (Figure 13), which was made through almost the entire thickness of the sample, showing that the recrystallization started from the edges of the printed plates, while the core of the sample is much less affected. The average grain size and aspect ratio by area fraction for IN718-B_4C are 165 μm and 0.20, respectively. Despite the significant visible changes, the IN718-B_4C variant still shows ≈45% fraction of VLAGBs and only a few percent of 60° twin boundaries, leading to the conclusion that the recrystallization process of IN718-B_4C

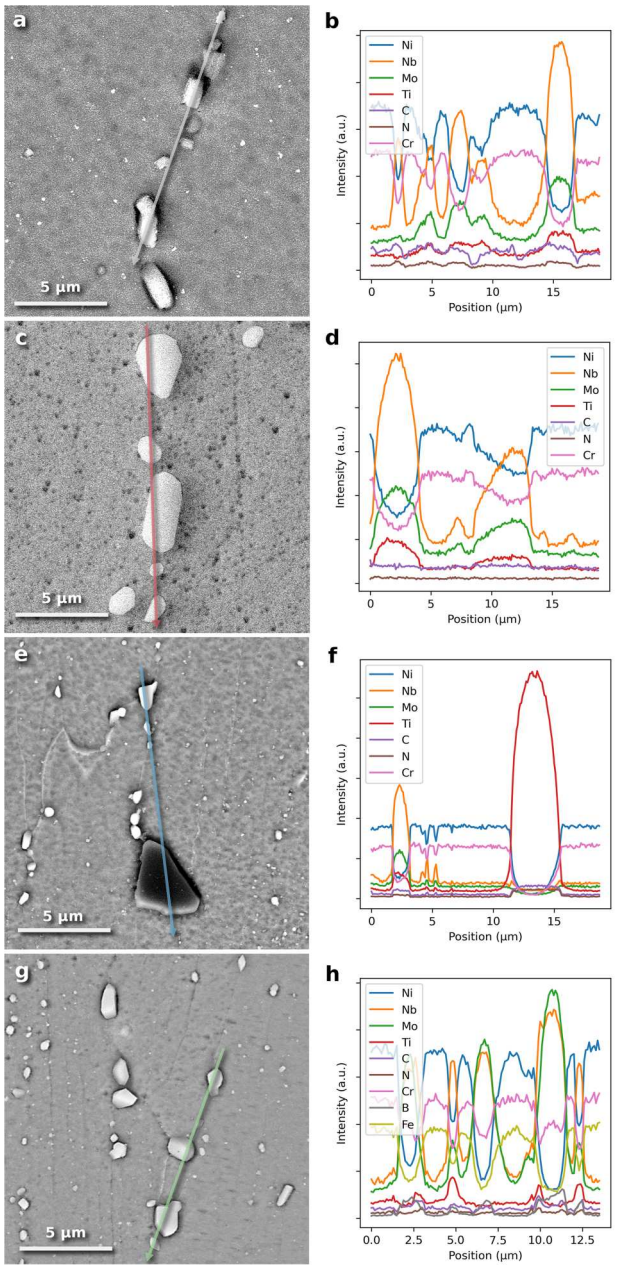

Figure 12. EDS line scans of Ni, Nb, C, Ti, N, and B (HDBSE micrographs and plotted intensities) for IN718 (a–b), IN718-NbC (c–d), IN718-TiC (e–f) and IN718-B_4C (g–h) after full HT.

would be similar to that of IN718 and IN718-NbC, but much slower.

3.6. Mechanical properties

Figure 15 shows Vickers hardness for different material variations. As-built samples are characterised by a hardness of 330–360 HV. Compared to the typical as-built hardness of PBF-LB/M-ed IN718 [41], IN718, IN718-NbC, IN718-TiC show almost the mean value, while IN718-B_4C is in the upper quartile of the results collected in the literature. After a full heat treatment (SA + HIP + SA + AA) the hardness increases to about 430 HV for pure IN718 and up to 460–485 HV for the IN718-TiC and IN718-NbC variants. IN718-TiC shows an increase in hardness in the BD plane up to 20 HV, due to the strong texture. Pure IN718, shows similar hardness to the homogenised and aged, wrought IN718 [32], as well as PBF-LB/M produced IN718 for the same condition (430–440 HV [41]). The addition of NbC and TiC increases the hardness by up to 50 HV above this average. Despite the high number of precipitates, IN718-B_4C does not show any improvement in hardness compared to pure IN718.

Hardness values close to 500 HV can be achieved for non-homogenised, heat treated, and aged IN718 after PBF-LB/M by maintaining residual microsegregation [3,62]. Additional factors that play a role in increased hardness are carbide size and density, microsegregation, possible residual dislocation cell structures, grain number and size, residual high number of LAGBs, effectiveness of solution annealing due to niobium concentration [3,45,63]. A higher concentration of niobium leads to more effective γ''/γ' precipitation. The increase in the number of precipitates may exceed the aging capacity of the IN718-B_4C alloy. Therefore, it can explain the higher hardness achieved for IN718-NbC and IN718-TiC, compared to IN718-B_4C, although the latter shows a higher volume of precipitates.

Figure 16 shows the yield strength (YS), ultimate tensile strength (UTS), and elongation at break for all material variants. Tensile curves are presented in Figure S4 in the supplementary material. IN718-B_4C is characterised by the lowest average UTS of 1,283 MPa, followed by pure IN718 at 1,317 MPa, IN718-TiC at 1,345 MPa, and IN718-NbC at 1,372 MPa. IN718-B_4C and pure IN718 show similar YS of 1,029 and 1,012 MPa, respectively, while IN718-TiC shows an increase in YS of over 100 MPa at 1,147 MPa, followed by IN718-NbC at 1,101 MPa. IN718-B_4C does not show improved properties compared to pure IN718, but IN718-TiC and IN718-NbC do. In addition, the typical UTS-ductility trade-off is not present here, as the elongation at break for pure IN718 averages 21.5% while it increases for each modified variant, i.e. for IN718-NbC it reaches 24.2%, for IN718-TiC it reaches 25.2% and for IN718-B_4C it reaches 22.9%. It should be noted that the YS and UTS obtained in this study are lower than in some other cases [18,28] due to the relatively large grain size (≈100 µm) and therefore the less significant Hall-Petch effect. However, all material variants exceed the minimum tensile properties for HT IN718 according to ASTM F3055-14a, i.e. minimum YS

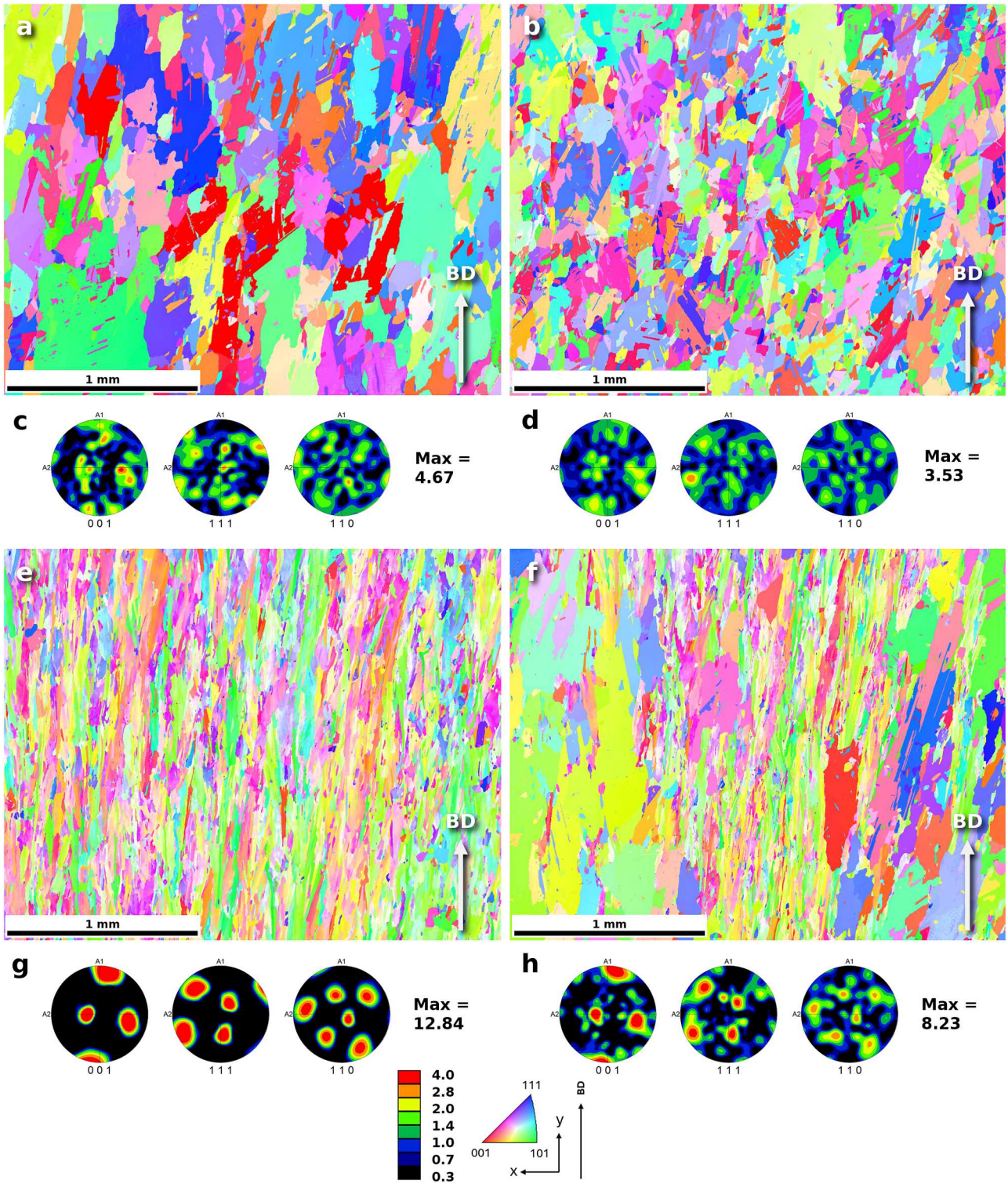

Figure 13. Inverse pole figure maps with colouring in the out-of-plane direction and corresponding pole figures for IN718 (a, c), IN718-NbC (b, d), IN718-TiC (e, g) and IN718-B_4C (f, h) after full HT.

of 920 MPa, UTS of 1,240 MPa, and elongation of 12%. It is important to note that carbide-modified variants exhibit significant improvement in ductility, while still showing improvements in the YS and UTS, as compared to the pure IN718.

Figure 17 presents kernel average misorientation (KAM) maps and geometrically necessary dislocation (GND) density distributions of fully heat-treated materials (Figure 13). The IN718 and IN718-NbC variants exhibited predominantly recrystallized grains, resulting

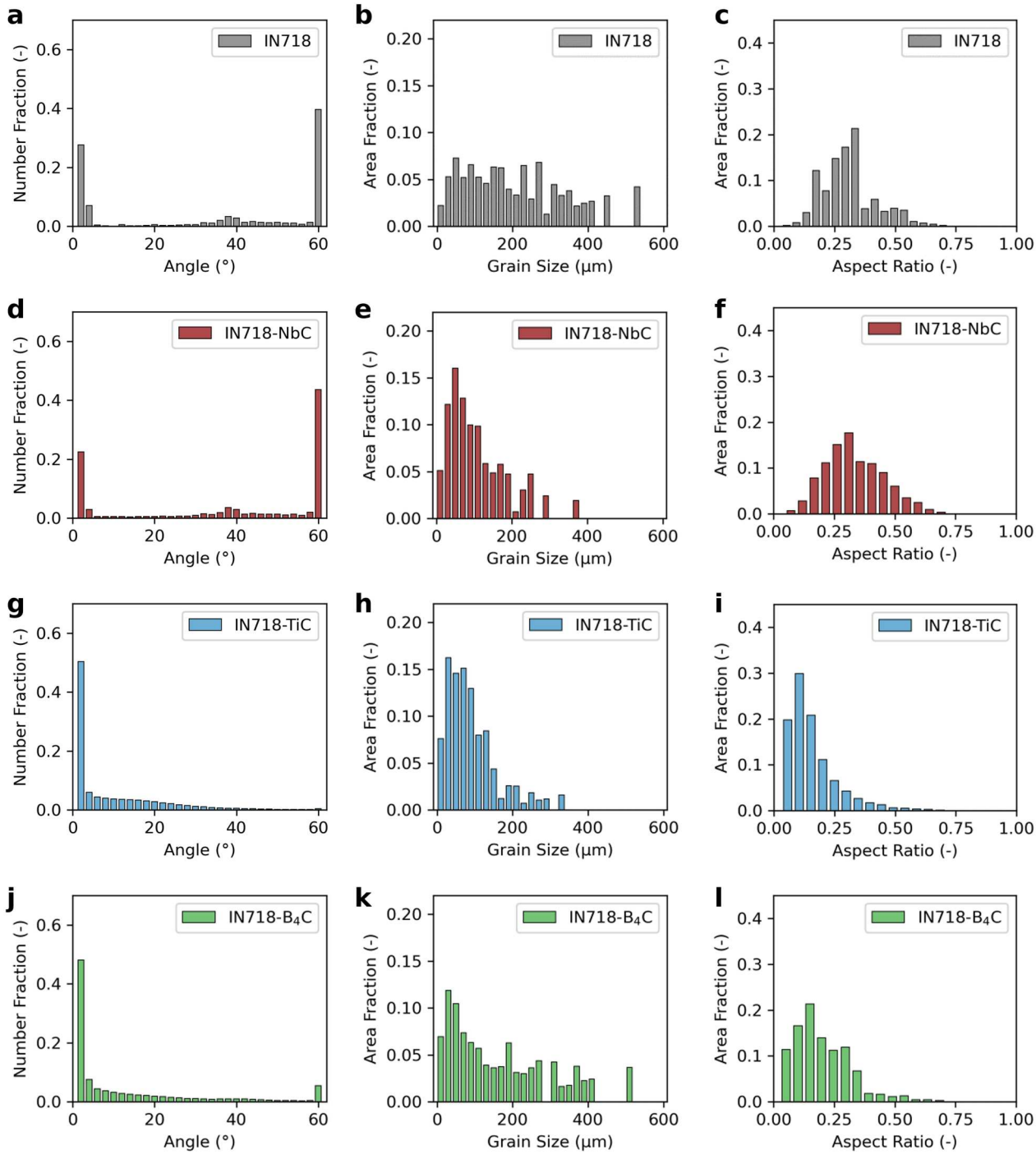

Figure 14. Bar plots of misorientation angle (a, d, g, j), grain aspect ratio (b, e, h, k), and grain size (c, f, i, l) for IN718 (a–c), IN718-NbC (d–f), IN718-TiC (d–f), and IN718-B_4C (d–f) after full HT.

in the lowest average GND densities (ρ) of $35{\cdot}10^{12}/m^2$ for IN718 and $45{\cdot}10^{12}/m^2$ for IN718-NbC. Furthermore, both variants exhibit relatively uniform GND density distributions, as illustrated in Figure 17(e and f). On the contrary, the non-recrystallized IN718-TiC variant displays a considerably higher $\rho = 15{\cdot}10^{13}/m^2$, yet its GND density distribution remains uniform across the captured area. The IN718-B_4C variant exhibits a combination of recrystallized and non-recrystallized grains within the EBSD scan area. This distinction is readily apparent in the KAM maps, wherein the recrystallized region exhibits markedly lower GND values. However, this is likely due to the higher proportion of small precipitates present in the non-recrystallized region of the IN718-TiC

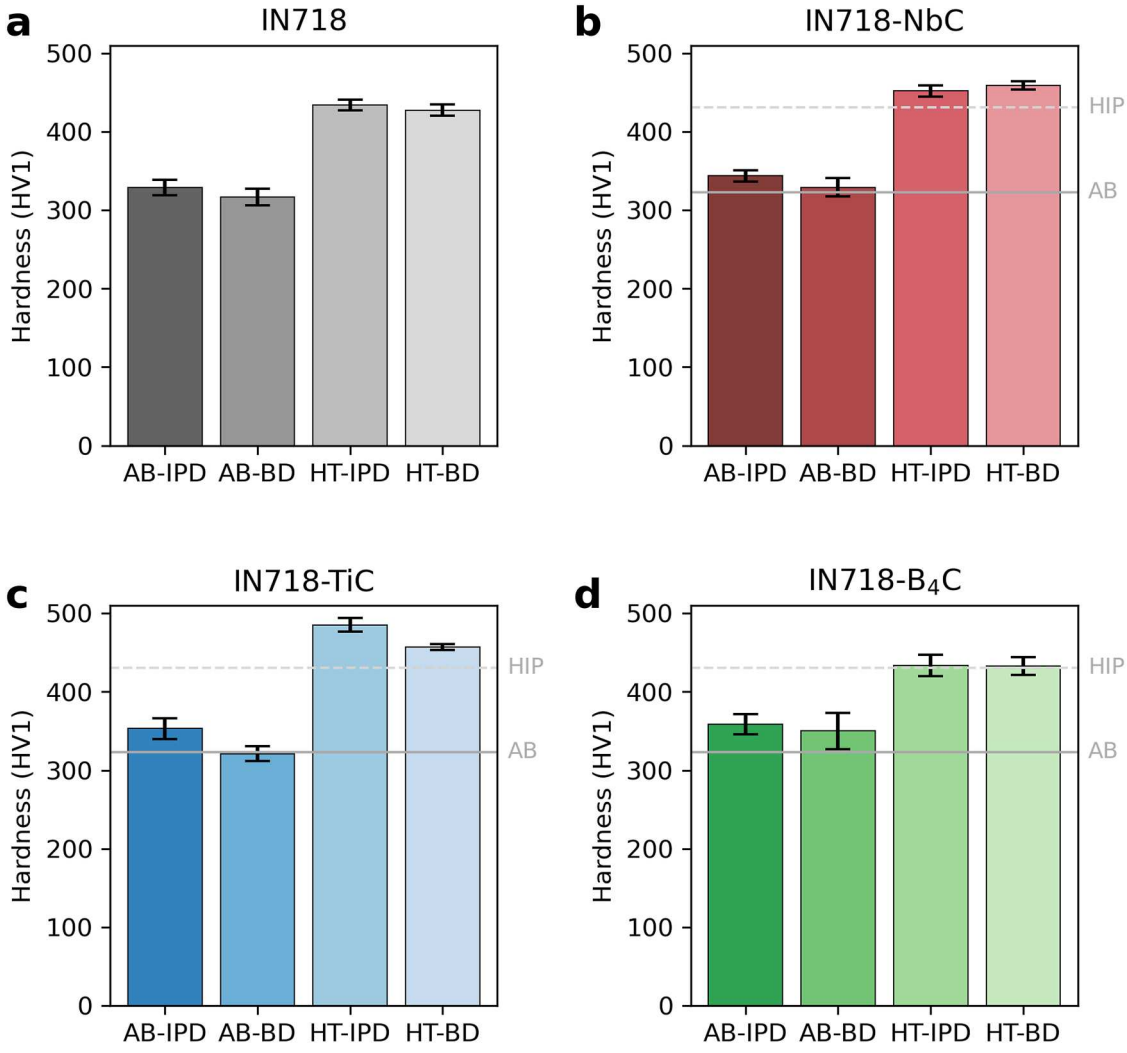

Figure 15. Vickers's microhardness of carbide-modified IN718, HV0.3; error bars – std deviation; IN718 (a), IN718-TiC (b), IN718-TiC (c), and IN718-B_4C (d) in as-built condition and after full HT and in both in plane (IPD) and build (BD) directions.

variant, compared to IN718-B4C variant (Figure 11). This results in a GND density reaching values of approximately $20{\cdot}10^{13}/m^2$, while the ρ is lower at $11{\cdot}10^{13}/m^2$.

To understand the contributions of various characteristics of the IN718 alloy and its carbide-modified variants, analytical equations were used to calculate the strengthening contributions. The following strengthening mechanisms can be considered for calculations: intrinsic strength of pure Ni (σ_0), solid solution strengthening (σ_{ss}), grain boundary strengthening (σ_{gb}), twin boundary strengthening (σ_{tb}), dislocation strengthening (σ_d), and precipitation strengthening (σ_p) [64]. Since the chemical composition of the variants differs by 0.6 wt.% or less, the intrinsic and solid solution strengthening contributions are nearly identical across all variants and can be neglected. The primary differences in strengthening arise from variations in grain size, precipitates, and dislocation density. Consequently, the contributions of grain boundary strengthening, dislocation strengthening, and precipitation strengthening to the overall strength were calculated. The specific equations and constants used for these calculations are detailed in the supplementary material (Tables S1–S2 and Equations S1–S3). The results of the calculations are presented in Table 8. To summarise the strengthening contribution of combined features, the difference between carbide-modified variants and the reference IN718 variant was calculated.

The results from the calculations indicate a good alignment between the calculated and measured differences for the IN718 and IN718-NbC variants. This similarity is attributed to the high degree of similarity between the microstructures of the two variants. The addition of 0.6 wt.% NbC results in a notable increase in the area fraction of carbides, from 0.29% in IN718 to 0.69% in IN718-NbC (see Figure 11). Given that the Nb content in pure IN718 is approximately 5 wt.%, the

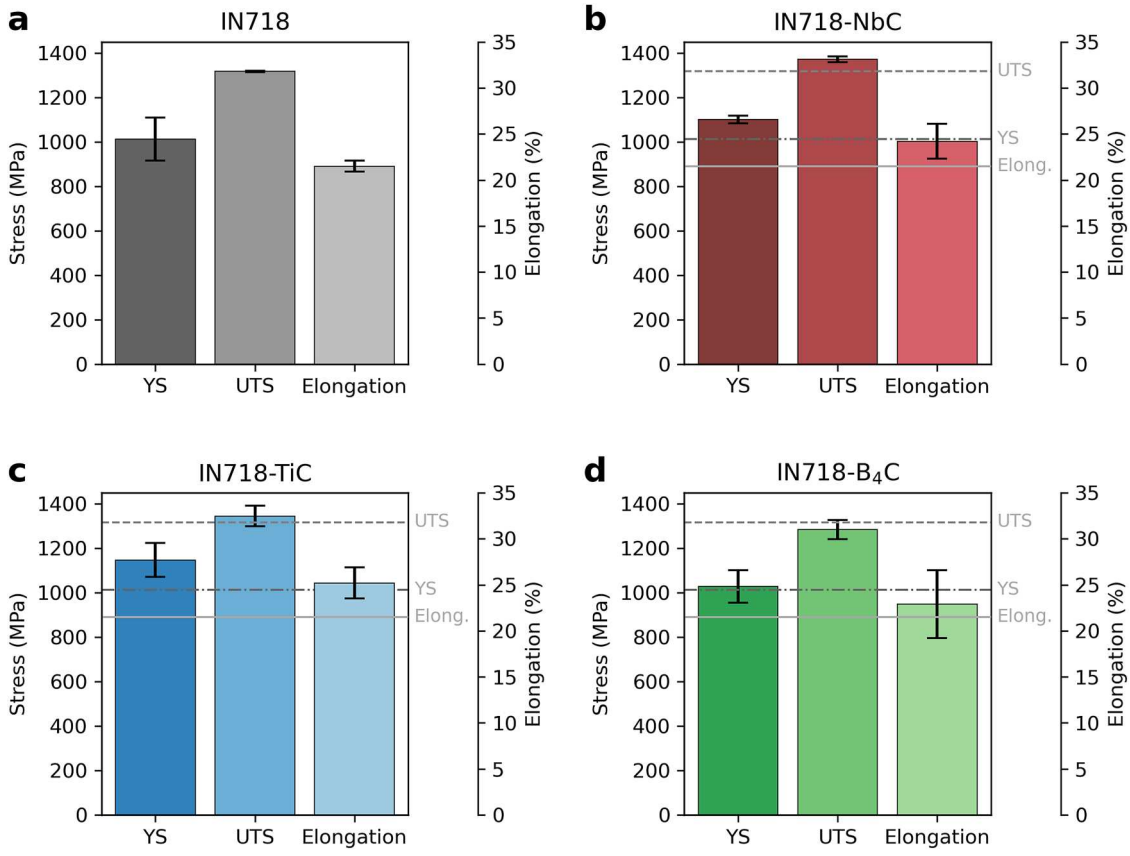

Figure 16. Yield strength, ultimate tensile strength, and elongation at break of carbide-modified IN718; error bars – std deviation; IN718 (a), IN718-NbC (b), IN718-TiC (c) and IN718-B_4C (d) after full HT.

increase in carbides relative to the increased Nb content (from 4.84 to 5.48 wt.%, as shown in Table 7). Therefore, the added Nb will compensate for its availability for γ″ (Ni_3Nb) formation during aging, which is the primary strengthening phase of the IN718 alloy [3].

Literature shows that the strength of the PBF-LB/M fabricated IN718 alloy after homogenisation and aging is mainly due to coherency strengthening by γ″, estimated at ≈830 MPa [64]. This explains the difference between analytical calculations and measured UTS for IN718-TiC, IN718-B_4C, and pure IN718. Calculations indicate strength increase via dislocations and Orowan strengthening, but measured results show a decrease in UTS for IN718-B_4C and a small increase for IN718-TiC. This is likely due to the lower fraction of γ″ after aging, as Nb, being the main element in carbides and carbide-nitrides, reduces its availability for γ″ formation. The increase in carbides and carbide-nitrides from 0.29% to 1.14% (IN718-TiC) and 2.29% (IN718-B_4C) consumes 0.5–1 wt.% Nb (10–20% of available Nb), reducing the γ″ fraction and lowering the strengthening contribution. Hardness measurements (Figure 15) support these conclusions, showing similar hardness for IN718-TiC and IN718-NbC, and lower hardness for IN718-B_4C despite higher carbide precipitate fractions.

Another significant factor differentiating IN718/IN718-NbC and IN718-TiC/IN718-B_4C is the grain morphology and crystallographic texture. In this study, tensile samples were fabricated with their main axes parallel to the build platform, making the loading direction perpendicular to the elongated grains in IN718-TiC and IN718-B_4C. An equiaxed-grained alloy generally has higher tensile strength when the tensile direction is perpendicular to the main axis of elongated grains in a directionally solidified alloy. This is because the elongated grain boundaries are more prone to sliding and failure, resulting in lower tensile strength when pulled along their length [65]. This effect is especially evident on the longitudinal surface of a tensile IN718-TiC sample (Figure 18), showing a distinct surface relief from grain boundary sliding, which causes crack initiation and propagation. Similar effects are observed for other carbide-modified variants, but to a lesser extent.

Moreover, all carbide-modified variants show higher elongation compared to pure IN718, which has less pronounced necking and more deformation relief on the

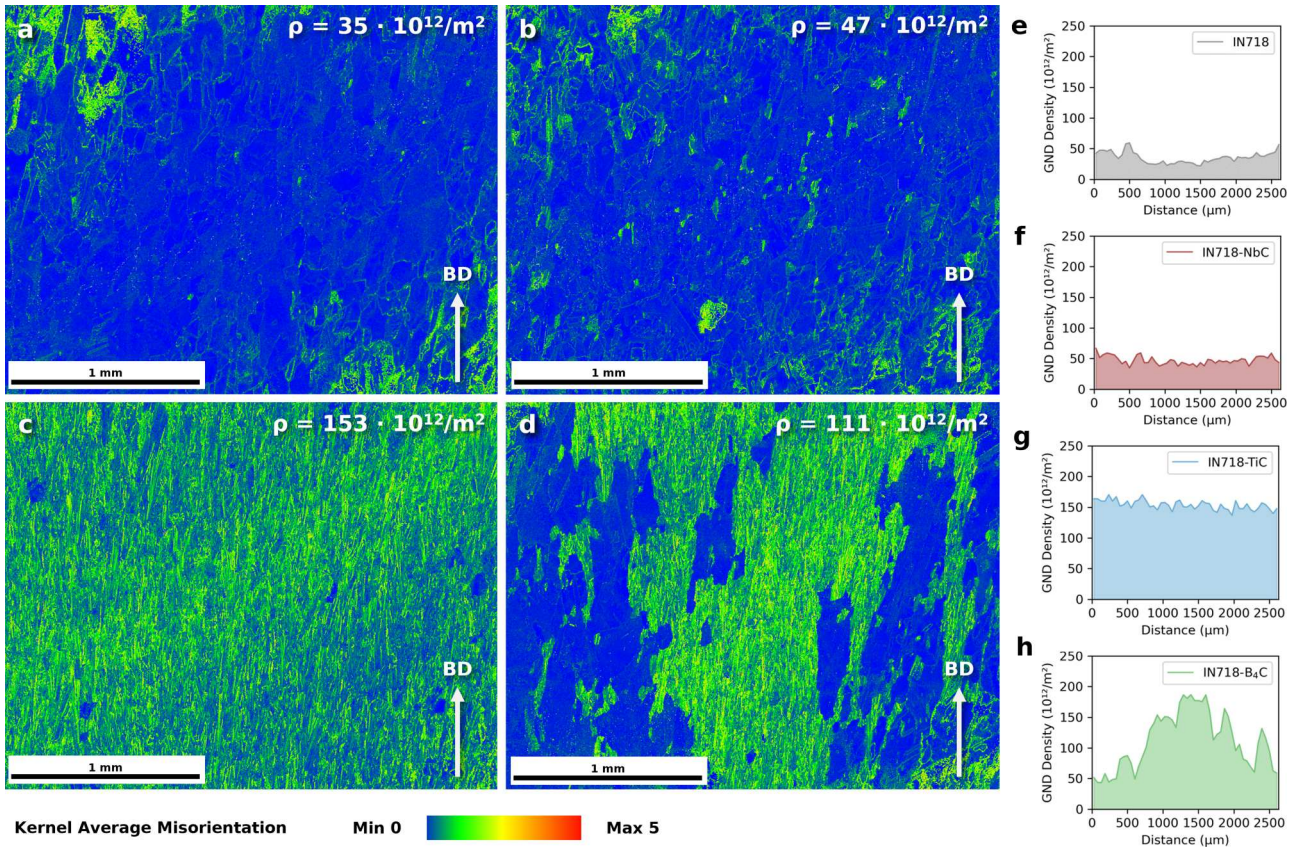

Figure 17. KAM maps (a–d) and GND density distribution (e–h) of IN718 (a, e), IN718-NbC (b, f), IN718-TiC (c, g) and IN718-B_4C (d, h) after full HT. KAM maps corresponds to IPF maps shown in Figure 13.

lateral surface (Figure 18(a)). Nano-sized carbides can effectively pin dislocations and shear particles [66], leading to dislocation annihilation, greater elongation, and reduced localised surface relief [66]. Carbides also influence the distribution of geometrically necessary dislocations, promoting homogeneous deformation and a better stress distribution [67], as supported by KAM maps and GND distribution plots (Figure 17). This conclusion is supported by the results of IN718-TiC, which exhibits the most uniform GND distribution, highest elongation, necking behaviour, and cross-sectional reduction.

The improved density of IN718 with carbide addition contrasts with previous studies. Key differences include the identification of large, brittle carbide inclusions as a major factor leading to lower ductility. These inclusions, especially if irregularly shaped and extensive, result in overall material brittleness due to unmelted, oversized particles [16,68] or smaller additive agglomerations [16]. Furthermore, Figures 5 and 9 illustrate the presence of oversized carbide inclusions in this particular work. However, these inclusions were isolated cases, ranging from ≈2–3 μm in IN718-B_4C to ≈20–30 μm in IN718-TiC (Figure 19). Fractures around inclusions show a typical ductile dimpled surface, with no major cleavage faces, indicating brittle behaviour. The large number of smaller carbides likely redistributed and associated strain around the scarce oversized

Table 8. Results of strengthening contribution calculations – equations and constants used are detailed in the supplementary material.

Parameter	IN718	IN718-NbC	IN718-TiC	IN718-B_4C
Grain boundary strengthening σ_{gb} (MPa)	65	84	90	64
Dislocation strengthening σ_d (MPa)	67	78	140	120
Orowan strengthening $\sigma_{Orowan\ (spheres)}$ (MPa)	75	109	144	127
Sum (MPa)	207	271	374	311
Calculated difference from IN718 (MPa)	N/A	+64	+167	+104
Measured difference from IN718 (MPa)	N/A	+55	+28	−34
Calculated-measured difference (MPa)	N/A	−9	−139	−138

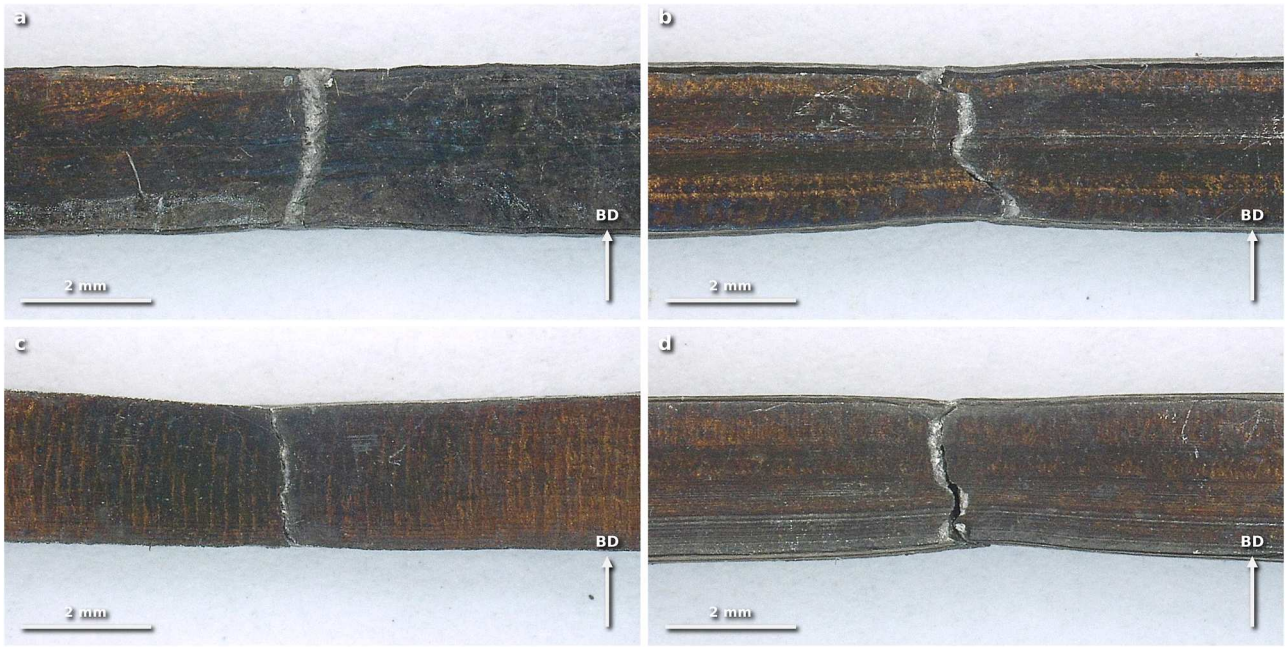

Figure 18. Micrographs of lateral surfaces of tensile samples after failure: IN718 (a); IN718-NbC (b); IN718-TiC (c); IN718-B_4C (d) after full HT.

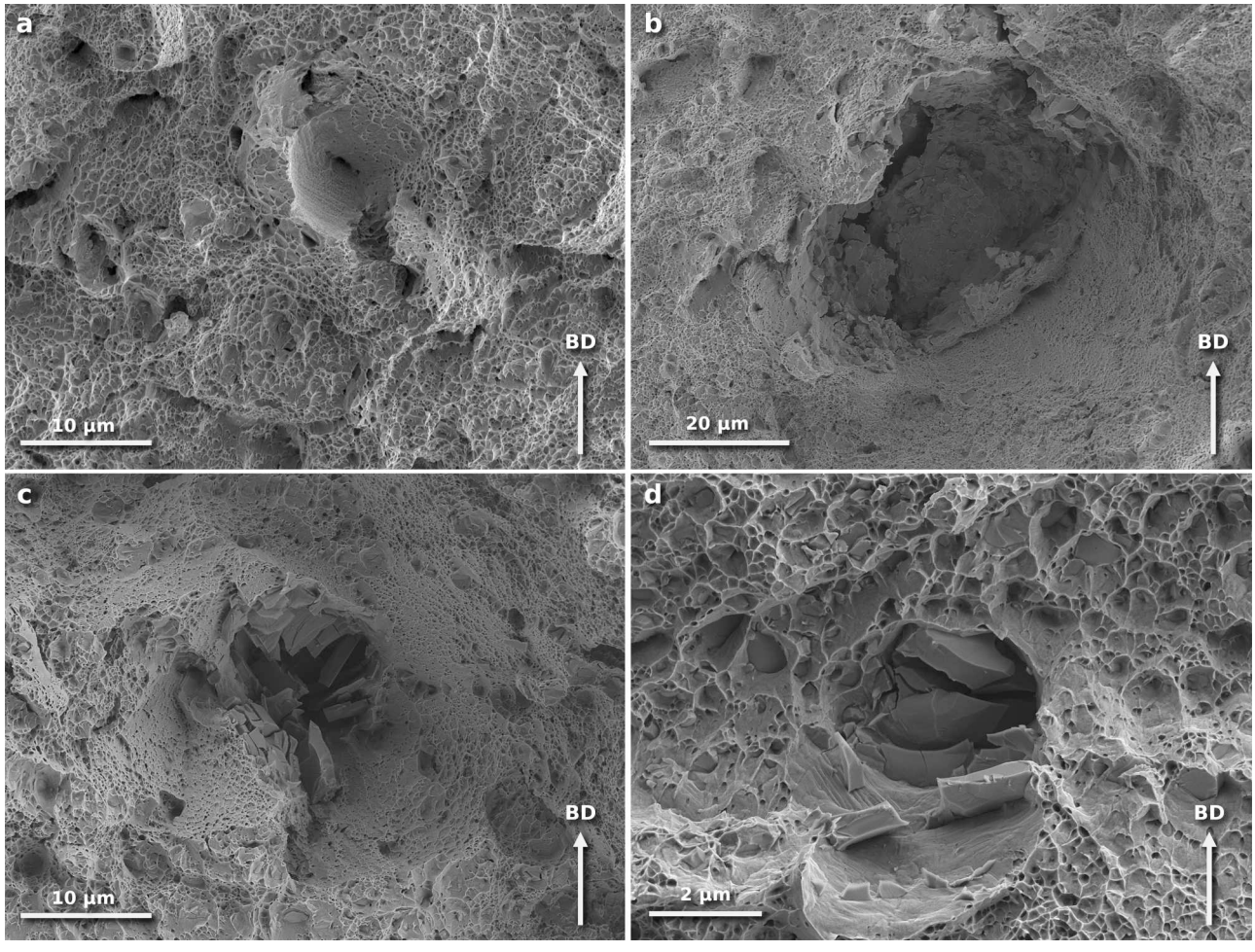

Figure 19. Micrographs (SEM, SE) of fracture surfaces of IN718 (a); IN718-NbC (b); IN718-TiC (c); IN718-B_4C (d) after full HT.

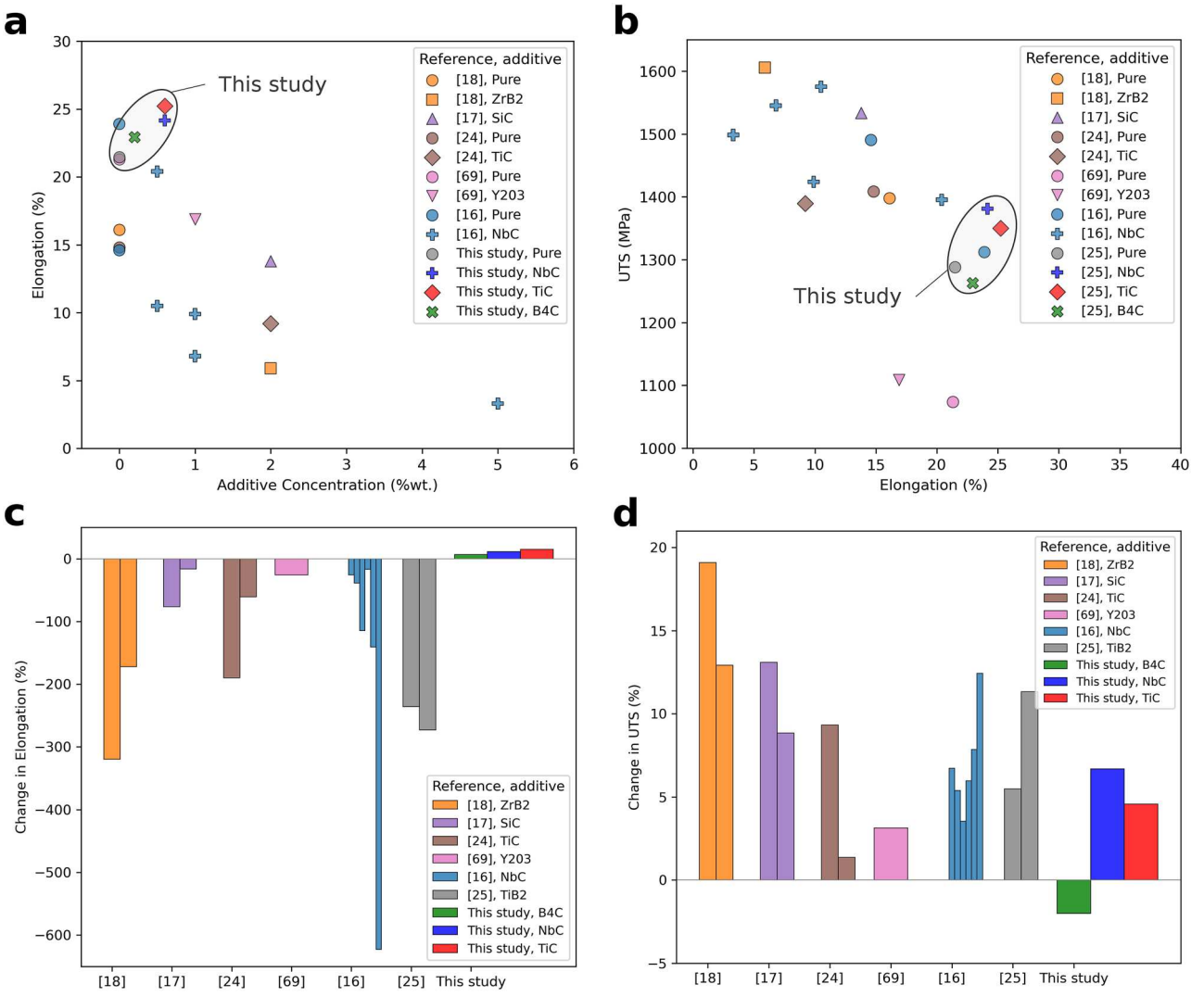

Figure 20. Comparison of RT tensile properties of modified IN718 in relation to the additive type and pure IN718; All materials after solution annealing and aging (SA + AA); (a) Elongation at break vs additive concentration; (b) UTS vs Elongation at break; (c) Elongation change by additive type; (f) UTS change by additive type; References: [16–18,24,25,69].

inclusions, and therefore does not significantly impact the overall alloy ductility. Nonetheless, excessive carbide addition will eventually reduce ductility beyond a certain threshold, as observed in IN718-B_4C. Although oversized carbides were not identified in IN718-B_4C due to the uniformity of the additive powder (Figure 2) and its lowest melting temperature, the overall ductility was lower than in other carbide-modified variants. This reduction is due to grain boundary precipitates forming a brittle, continuous film beyond a certain threshold, rather than evenly distributed pinned grain boundaries that aid in stress distribution and control dislocation movement [61].

Figure 20(a and b) shows a comparison of the RT tensile properties of carbide-modified IN718 of this study with differently modified IN718 form the literature. In the comparison, only materials after annealing and aging (SA + AA) are compared, to ensure consistent heat treatments. The effect of additive type on the elongation at break is compared in Figure 20(c), and the effect of additive type on the UTS in Figure 20(d). As different studies used different PBF-LB/M fabrication procedures, the materials in Figure 20(c and d) are related to their pure counterparts. A clear correlation between additive concentration and elongation is found (Figure 20(a)). With increasing additive concentration, the elongation drastically decreases. Figure 20(b) provides a clear overview of the possible pareto front in optimisation for UTS and elongation. It is worth noting that these results are for both cases on that front, which means that the UTS-elongation compromise for carbide-modified IN718 is improved compared to previous efforts.

Previous studies [16–18,24,25,69] have reported increases in room temperature tensile strength for modified IN718 ranging from <5% to 20% compared to unmodified counterparts, attributed to the Hall-Petch effect, finer grain sizes, additional carbide precipitates that hinder dislocation movement, and strong interfacial bonding between additives and the IN718 matrix [28]. However, for aerospace alloys, material properties such as fatigue resistance, toughness, and thermal strain accommodation, which are critical to operational reliability and directly related to ductility, outweigh mere improvements in tensile strength. Specifically, these studies have observed significant reductions in ductility due to factors such as large additive particle sizes [16], inadequate powder mixing [23,28], and suboptimal PBF-LB/M parameters [29], which can lead to material brittleness and cracking, particularly with irregular additive particle shapes [16]. Considering the above discussion on the influence of carbides on the ductility of PBF-LB/M fabricated IN718, the carbide addition threshold is probably below 1 wt.% for NbC or TiC and significantly lower for B_4C.

Our findings, however, indicate that with careful PBF-LB/M process design and TiC, NbC additives, it is feasible to refine the grain structure in IN718, achieving better yield strength and ultimate tensile strength without compromising the ductility. This was possible as a result of a multi-step and careful process design, including: (i) low carbide addition; (ii) powder mixing process focused on producing powder without carbide conglomerates; (iii) PBF-LB/M process parameters that allow almost complete dissolution of additives; (iv) post-process heat treatment with hot isostatic pressing densification; (v) grain control during the heat treatment process due enhanced pinning effect.

4. Conclusions

This study investigated a method for refining the grain structure of PBF-LB/M fabricated Inconel 718 and subsequent heat treatment, including hot isostatic pressing. Micron-sized powder carbides, NbC, TiC, and B_4C, were added at 0.6, 0.6, and 0.2 wt.%, respectively. The study aimed at complete melting of the additives during PBF-LB/M fabrication. The effects of carbide additives on IN718 processability by PBF-LB/M, microstructure, and room temperature tensile properties of the IN718 alloy were examined. The results demonstrate that careful optimisation of the PBF-LB/M process can achieve grain refinement and improved tensile strength while preserving tensile elongation. Using IN718 modified with carbides and subjected to HIP in compliance with aviation industry standards maintains excellent mechanical properties by suppressing grain coarsening and ensuring uniform stress distribution. The key findings are as follows:

- Carbide additives reduce IN718-carbide powder mixture flowability, but increase laser absorption. The PBF-LB/M parameters can be maintained for low carbide concentrations. Micron-sized carbide powder particles (1–3 µm) are fully melted at an energy density of 117.9 J/mm^3. Larger particles should be avoided.
- Pure IN718 undergoes significant grain growth during heat treatment, while addition of NbC refines grain size, and addition of TiC enhances Zener pinning at the dendritic cell level, maintaining the as-built texture. The addition of B_4C slows recrystallization, resulting in a heterogeneous texture with larger and more complex carbides and diborides. This differs from the more uniform carbide precipitates observed in the IN718, IN718-NbC, and IN718-TiC variants, each at different volume fractions.
- The addition of NbC and TiC increases the Vickers hardness of IN718 after heat treatment by about 10%, while the addition of B_4C shows no change in hardness. IN718-NbC and IN718-TiC show a 10% increase in yield strength and ultimate tensile strength compared to pure IN718. In contrast, IN718-B_4C shows no improvement. Additions of TiC and NbC result in up to 15% higher elongation at break compared to pure IN718.
- The primary differences in tensile behaviour arises from variations in grain size, texture, precipitates, and dislocation density. In IN718-TiC and IN718-NbC, the presence of carbides leads to uniform GND distribution and promotes uniform stress distribution. As a result, the trade-off between strength and ductility in carbide-modified IN718 is overcome compared to pure IN718.

Acknowledgements

Konrad Gruber extends his gratitude to Prof. Dr. Markus Strobl for hosting in the Applied Materials Group (Laboratory for Neutron Scattering and Imaging, Paul Scherrer Institute), and to Dr. Bogumiła Kuźnicka for discussions that enriched this work.

Disclosure statement

No potential conflict of interest was reported by the author(s).

Funding

This work was supported by the National Science Centre Poland (NCN) [Narodowe Centrum Nauki] under the MINIATURA 6 programme (grant number 2022/06/X/ST5/00725).

Data availability statement

The data that support the findings of this study are available from the corresponding author upon reasonable request.

References

[1] Munsch M, Schmidt-Lehr M, Wycisk E, et al.. Additive manufacturing market report. Hamburg: AMPOWER GmbH & Co. KG; 2023.

[2] Han C, Zhou K. *Metal powder-based additive manufacturing*. Weinheim: WILEY-VCH; 2023.

[3] Gruber K, Dziedzic R, Kuźnicka B, et al. Impact of high temperature stress relieving on final properties of Inconel 718 processed by laser powder bed fusion. Mater Sci Eng A. 2021;813(2021) 141111 Contents:1–15. doi:10.1016/j.msea.2021.141111

[4] Schafrik RE, Ward DD, Groh JR. Application of alloy 718 in GE aircraft engines: past, present and next five years. In Proceedings of the International Symposium on Superalloys and Various Derivatives; The Minerals, Metals & Materials Society; 2001. p. 11. doi:10.7449/2001/superalloys_2001_1_11

[5] Zeng Z, Gao S, Pokkalla DK, et al. Additive manufacturing of metallic metamaterials with enhanced mechanical properties enabled by microstructural and structural design. Int J Mach Tools Manuf. 2024 Jun;199:104172. doi:10.1016/j.ijmachtools.2024.104172

[6] Han C, Fang Q, Shi Y, et al. Recent advances on high-entropy alloys for 3D printing. Adv Mater. 2020 Jul 1;32 (26). doi:10.1002/adma.201903855

[7] Zhang D, Prasad A, Bermingham MJ, et al. Grain refinement of alloys in fusion-based additive manufacturing processes. Metall Mater Trans A Phys Metall Mater Sci. 2020 Sep;51(9):4341–4359. doi:10.1007/s11661-020-05880-4

[8] Xiong Y, Du J, Wei X, et al. Grain refinement of superalloy IN718C by the addition of inoculants. Metall Mater Trans A Phys Metall Mater Sci. 2004;35A(7):2111–2114. doi:10.1007/s11661-004-0159-8

[9] Liu L, Huang T, Xiong Y, et al. Cast structure and mechanical properties of fine grained superalloy K4169 by addition of refiners. Proc Int Symp Superalloys. 2004:493–500. doi:10.7449/2004/superalloys_2004_493_500

[10] Martin JH, Yahata BD, Hundley JM, et al. 3D printing of high-strength aluminium alloys. Nature. 2017;549 (7672):365–369. doi:10.1038/nature23894

[11] Duan R, Li S, Cai B, et al. In situ alloying based laser powder bed fusion processing of β Ti–Mo alloy to fabricate functionally graded composites. Compos B Eng. 2021 Oct;222:109059. doi:10.1016/j.compositesb.2021.109059

[12] Zhai W, Zhou W, Nai SML. Grain refinement of 316L stainless steel through in-situ alloying with Ti in additive manufacturing. Mater Sci Eng A. 2022 Apr;840:142912. doi:10.1016/j.msea.2022.142912

[13] Ho IT, Chen YT, Yeh AC, et al. Microstructure evolution induced by inoculants during the selective laser melting of IN718. Addit Manuf. 2018;21(April):465–471. doi:10.1016/j.addma.2018.02.018

[14] Ho IT, Hsu T-H, Chang Y-J, et al. Effects of CoAl2O4 inoculants on microstructure and mechanical properties of IN718 processed by selective laser melting. Addit Manuf. 2020;35(December 2019):101328. doi:10.1016/j.addma.2020.101328

[15] Hsu T-H, Chang K-C, Chang Y-J, et al. Effect of carbide inoculants additions in IN718 fabricated by selective laser melting process. In: Tin S, Hardy M, Clews J, Cormier J, Feng Q, Marcin J, O'Brien C, Suzuki A, editors. *Superalloys 2020*. Cham: Springer International Publishing; 2020. p. 982–989.

[16] Chang KC, Lee M-Y, Hsu T-H, et al. An effective strengthening strategy of nano carbide precipitation and cellular microstructure refinement in a superalloy fabricated by selective laser melting process. Metals (Basel). 2021 Nov;11(11):1691. doi:10.3390/met11111691

[17] Tekoğlu E, O'Brien AD, Liu J, et al. Strengthening additively manufactured Inconel 718 through in-situ formation of nanocarbides and silicides. Addit Manuf. 2023 Apr;67:103478. doi:10.1016/j.addma.2023.103478

[18] Tekoğlu E, O'Brien AD, Bae J-S, et al. Metal matrix composite with superior ductility at 800°C: 3D printed In718 + ZrB2 by laser powder bed fusion. Compos B Eng. 2024 Jan;268:111052. doi:10.1016/j.compositesb.2023.111052

[19] Kontis P, Alabort E, Barba D, et al. On the role of boron on improving ductility in a new polycrystalline superalloy. Acta Mater. 2017 Feb;124:489–500. doi:10.1016/j.actamat.2016.11.009

[20] Xiao S, Liang Z, Zheng Y, et al. The tensile creep behavior of a B4C-bearing high Nb containing TiAl alloy. Intermetallics (Barking). 2022 Feb;141:107410. doi:10.1016/j.intermet.2021.107410

[21] Xu Z, Xie Y, Ebrahimnia M, et al. Effect of B4C nanoparticles on microstructure and properties of laser cladded IN625 coating. Surf Coat Technol. 2021 Jun;416:127154. doi:10.1016/j.surfcoat.2021.127154

[22] Li Y, Zhang D, Zhao B, et al. In situ synthesis and characterization of ceramic reinforced Inconel 718 coatings using B4C-Inconel 718 powders by laser-directed energy deposition. Int J Adv Manuf Technol. 2022 Jun;120(7–8):5193–5203. doi:10.1007/s00170-022-09069-4

[23] Mandal V, Tripathi P, Kumar A, et al. A study on selective laser melting (SLM) of TiC and B4C reinforced IN718 metal matrix composites (MMCs). J Alloys Compd. 2022 Apr;901:163527. doi:10.1016/j.jallcom.2021.163527

[24] Yao X, Moon SK, Lee BY, et al. Effects of heat treatment on microstructures and tensile properties of IN718/TiC nanocomposite fabricated by selective laser melting. Int J Prec Eng Manuf. 2017 Dec;18(12):1693–1701. doi:10.1007/s12541-017-0197-y

[25] Zhao M, Song J, Tang Q, et al. Laser powder bed fusion of Inconel 718-based composites: effect of TiB2 content on microstructure and mechanical performance. Opt Laser Technol. 2023 Dec;167:109596. doi:10.1016/j.optlastec.2023.109596

[26] Markanday JFS, Carpenter MA, Thompson RP, et al. Effect of NbC inoculants on the elastic properties and microstructure of additively manufactured IN718. Materialia (Oxf). 2023 Mar;27:101701. doi:10.1016/j.mtla.2023.101701

[27] Tiparti D, Ho IT, Chang KC, et al. Understanding the effects of CoAl2O4 inoculant additions on microstructure in

additively manufactured Inconel 718 processed via selective laser melting. Metall Mater Trans A Phys Metall Mater Sci. 2021;52(6):2630–2641. doi:10.1007/s11661-021-06255-z

[28] Gu D, Zhang H, Dai D, et al. Laser additive manufacturing of nano-TiC reinforced Ni-based nanocomposites with tailored microstructure and performance. Compos B Eng. 2019 Apr;163:585–597. doi:10.1016/j.compositesb.2018.12.146

[29] Yuan P, Gu D, Dai D. Particulate migration behavior and its mechanism during selective laser melting of TiC reinforced Al matrix nanocomposites. Mater Des. 2015 Oct;82:46–55. doi:10.1016/j.matdes.2015.05.041

[30] Xu JQ, Chen LY, Choi H, et al. Theoretical study and pathways for nanoparticle capture during solidification of metal melt. J Phys Condens Matter. 2012 Jun;24(25):255304. doi:10.1088/0953-8984/24/25/255304

[31] DuPont JN, Lippold JC, Kiser SD. *Welding metallurgy and weldability of nickel-base alloys*. Hoboken (NJ): John Wiley & Sons, Inc. All; 2009. doi:10.1002/9780470500262

[32] Gruber K, Stopyra W, Kobiela K, et al. Mechanical properties of Inconel 718 additively manufactured by laser powder bed fusion after industrial high-temperature heat treatment. J Manuf Process. 2022;73(January 2022):642–659. doi:10.1016/j.jmapro.2021.11.053

[33] Gruber K, Smolina I, Kasprowicz M, et al. Evaluation of Inconel 718 metallic powder to optimize the reuse of powder and to improve the performance and sustainability of the Laser Powder Bed Fusion (LPBF) process. Materials (Basel). 2021;14(1538):1–27. doi:10.3390/ma14061538.

[34] Gruber K, Smolina I, Stopyra W. Assessing metal powder quality for additive manufacturing using diffuse light spectroscopy. Powder Technol. 2024 Feb;434:119366. doi:10.1016/j.powtec.2024.119366

[35] Zhang D, Feng Z, Wang C, et al. Comparison of microstructures and mechanical properties of Inconel 718 alloy processed by selective laser melting and casting. Mater Sci Eng A. 2018 May;724:357–367. doi:10.1016/j.msea.2018.03.073

[36] Pawlak A, Szymczyk PE, Kurzynowski T, et al. Selective laser melting of magnesium AZ31B alloy powder. Rapid Prototyp J. 2020 Feb;26(2):249–258. doi:10.1108/RPJ-05-2019-0137

[37] Luu DN, Zhou W, Nai SML, et al. Mitigation of solute segregation during solutionization of selective laser melted Inconel 718 through micron-TiC addition. J Alloys Compd. 2022 Mar;897:163224. doi:10.1016/j.jallcom.2021.163224

[38] Cao WD, Kennedy RL, Willis MP. Differential Thermal Analysis (DTA) study of the homogenization process in alloy 718. Superalloys 718, 625 Various Derivatives. 1991:147–160. doi:10.7449/1991/superalloys_1991_147_160

[39] Volpato GM, Tetzlaff U, Fredel MC. A comprehensive literature review on laser powder bed fusion of Inconel superalloys. Addit Manuf. 2022 Jul 1;55:102871, Elsevier B.V. doi:10.1016/j.addma.2022.102871

[40] Sanchez S, Smith P, Xu Z, et al. Powder Bed Fusion of nickel-based superalloys: A review. Int J Mach Tools Manuf. 2021 Jun 1;165:103729, Elsevier Ltd. doi:10.1016/j.ijmachtools.2021.103729

[41] Hosseini E, Popovich VAA. A review of mechanical properties of additively manufactured Inconel 718. Addit Manuf. 2019;30:100877. doi:10.1016/j.addma.2019.100877

[42] Balasubramanian S, Philpott C, Hyder J, et al. Testing techniques and fatigue of additively manufactured Inconel 718 – a review. Int J Eng Mater Manuf. 2020;5(4):156–194. doi:10.26776/ijemm.05.04.2020.05

[43] Wang X, Gong X, Chou K. Review on powder-bed laser additive manufacturing of Inconel 718 parts. Proc Inst Mech Eng B J Eng Manuf. 2017;231(11):1890–1903. doi:10.1177/0954405415619883

[44] Tucho WM, Cuvillier P, Sjolyst-Kverneland A, et al. Microstructure and hardness studies of Inconel 718 manufactured by selective laser melting before and after solution heat treatment. Mater Sci Eng A. 2017;689:220–232. doi:10.1016/j.msea.2017.02.062

[45] Gallmeyer TG, Moorthy S, Kappes BB, et al. Knowledge of process-structure-property relationships to engineer better heat treatments for laser powder bed fusion additive manufactured Inconel 718. Addit Manuf. 2020;31:100977. doi:10.1016/j.addma.2019.100977

[46] Afrasiabi M, Keller D, Lüthi C, et al. Effect of process parameters on melt pool geometry in laser powder bed fusion of metals: a numerical investigation. Procedia CIRP. 2022;113:378–384, Elsevier B.V. doi:10.1016/j.procir.2022.09.187

[47] Khairallah SA, Anderson AT, Rubenchik A, et al. Laser powder-bed fusion additive manufacturing: physics of complex melt flow and formation mechanisms of pores, spatter, and denudation zones. Acta Mater. 2016 Apr;108:36–45. doi:10.1016/j.actamat.2016.02.014

[48] Xiao H, Li S, Han X, et al. Laves phase control of Inconel 718 alloy using quasi-continuous-wave laser additive manufacturing. Mater Des. 2017;122:330–339. doi:10.1016/j.matdes.2017.03.004

[49] Wang W, Zhu C, Zeng J, et al. Microstructures and Nb-rich precipitation behaviors of Inconel 718 Superalloy under sub-rapid solidification process. Metall Mater Trans A Phys Metall Mater Sci. 2020 May;51(5):2306–2317. doi:10.1007/s11661-020-05696-2

[50] Sohrabi MJ, Mirzadeh H. Revisiting the diffusion of niobium in an as-cast nickel-based Superalloy during annealing at elevated temperatures. Met Mater Int. 2020 Mar;26(3):326–332. doi:10.1007/s12540-019-00342-y

[51] Zhao Y, Li K, Gargani M, et al. A comparative analysis of Inconel 718 made by additive manufacturing and suction casting: microstructure evolution in homogenization. Addit Manuf. 2020;36:101404. doi:10.1016/j.addma.2020.101404

[52] Silva CC, De Miranda HC, Motta MF, et al. New insight on the solidification path of an alloy 625 weld overlay. J Mater Res Technol. 2013;2(3):228–237. doi:10.1016/j.jmrt.2013.02.008

[53] Lim KH, Ryou K, Choi J-H, et al. Effect of titanium nitride inclusions on the mechanical properties of direct laser deposited Inconel 718. Extreme Mech Lett. 2023 Jun;61:102009. doi:10.1016/j.eml.2023.102009

[54] Wolff L, Bastin G, Heijligers H. The titanium-nitrogen system. Solid State Ion. 1985;16:105–112. doi:10.1016/0167-2738(85)90031-1

[55] Kindermann RM, Roy MJ, Morana R, et al. Process response of Inconel 718 to wire + arc additive manufacturing with cold metal transfer. Mater Des. 2020 Oct;195:109031. doi:10.1016/j.matdes.2020.109031

[56] McLouth TD, Bean GE, Witkin DB, et al. The effect of laser focus shift on microstructural variation of Inconel 718 produced by selective laser melting. Mater Des. 2018;149:205–213. doi:10.1016/j.matdes.2018.04.019

[57] Wang Y, Shi J. Developing very strong texture in a nickel-based superalloy by selective laser melting with an ultra-high power and flat-top laser beam. Mater Charact. 2020 Jul;165:110372. doi:10.1016/j.matchar.2020.110372

[58] Theska F, Tse WF, Schulz B, et al. Review of Microstructure–mechanical property relationships in cast and wrought Ni-based superalloys with boron, carbon, and zirconium microalloying additions. Adv Eng Mater. 2022;25; doi:10.1002/adem.202201514

[59] Ghaemifar S, Mirzadeh H. Precipitation kinetics of niobium carbide (NbC) during homogenization heat treatment of additively manufactured Inconel 718 superalloy. J Mater Re Technol. 2023 Jul;25:1774–1781. doi:10.1016/j.jmrt.2023.06.069

[60] Vernier S, Pugliara A, Viguier B, et al. Solid-state phase transformations involving (Nb,Mo)2CrB2 borides and (Nb,Ti)2CS carbosulfides at the grain boundaries of superalloy Inconel 718. Metall Mater Trans A Phys Metall Mater Sci. 2020 Dec;51(12):6607–6629. doi:10.1007/s11661-020-06045-z

[61] Kontis P, Yusof HAM, Pedrazzini S, et al. On the effect of boron on grain boundary character in a new polycrystalline superalloy. Acta Mater. 2016 Jan;103:688–699. doi:10.1016/j.actamat.2015.10.006

[62] Gruber K, Szymczyk-Ziółkowska P, Dziuba S, et al. Fatigue crack growth characterization of Inconel 718 after additive manufacturing by laser powder bed fusion and heat treatment. Int J Fatigue. 2023;166(January 2023):107287. doi:10.1016/j.ijfatigue.2022.107287

[63] Fayed EM, Shahriari D, Saadati M, et al. Influence of homogenization and solution treatments time on the microstructure and hardness of Inconel 718 fabricated by laser powder bed fusion process. Materials (Basel). 2020;13(11):23. doi:10.3390/ma13112574

[64] Zhang S, Lin X, Wang L, et al. Strengthening mechanisms in selective laser-melted Inconel718 superalloy. Mater Sci Eng A. Apr. 2021;812:141145. doi:10.1016/j.msea.2021.141145

[65] Ni M, Chen C, Wang X, et al. Anisotropic tensile behavior of in situ precipitation strengthened Inconel 718 fabricated by additive manufacturing. Mater Sci Eng A. 2017;701:344–351. doi:10.1016/j.msea.2017.06.098

[66] Kamikawa N, Sato K, Miyamoto G, et al. Stress-strain behavior of ferrite and bainite with nano-precipitation in low carbon steels. Acta Mater. 2015 Jan;83:383–396. doi:10.1016/j.actamat.2014.10.010

[67] Karamched PS, Wilkinson AJ. High resolution electron back-scatter diffraction analysis of thermally and mechanically induced strains near carbide inclusions in a superalloy. Acta Mater. 2011 Jan;59(1):263–272. doi:10.1016/j.actamat.2010.09.030

[68] Shen MY, Tian XJ, Liu D, et al. Microstructure and fracture behavior of TiC particles reinforced Inconel 625 composites prepared by laser additive manufacturing. J Alloys Compd. 2018;734:188–195. doi:10.1016/j.jallcom.2017.10.280

[69] Song Q, Zhang Y, Wei Y-f, et al. Microstructure and mechanical performance of ODS superalloys manufactured by selective laser melting. Opt Laser Technol. 2021 Dec;144:107423. doi:10.1016/j.optlastec.2021.107423